Differential Kras^V12 protein levels control a switch regulating lung cancer cell morphology and motility

C. Schäfer[1,2], **A. Mohan**[1], **W. Burford**[1], **M. K. Driscoll**[1], **A. T. Ludlow**[1], **W. E. Wright**[1], **J. W. Shay**[1], and **G. Danuser**[1,*]

[1]Department of Cell Biology, University of Texas Southwestern Medical Center, 5323 Harry-Hines Blvd, Dallas, Texas 75390

Abstract

Introduction—Oncogenic Kras mutations are important drivers of lung cancer development and metastasis. They are known to activate numerous cellular signaling pathways implicated in enhanced proliferation, survival, tumorigenicity and motility during malignant progression.

Objectives—Most previous studies of Kras in cancer have focused on the comparison of cell states in the absence or presence of oncogenic Kras mutations. Here we show that differential expression of the constitutively active mutation Kras^V12 has profound effects on cell morphology and motility that drive metastatic processes.

Methods—The study relies on lung cancer cell transformation models, patient-derived lung cancer cell lines, and human lung tumor sections combined with molecular biology techniques, live-cell imaging and staining methods.

Results—Our analysis shows two cell functional states driven by Kras^V12 protein levels: a non-motile state associated with high Kras^V12 levels and tumorigenicity, and a motile state associated with low Kras^V12 levels and cell dissemination. Conversion between the states is conferred by differential activation of a mechano-sensitive double-negative feedback between Kras^V12/ERK/ Myosin II and matrix-adhesion signaling. Kras^V12 expression levels change upon cues such as hypoxia and integrin-mediated cell-matrix adhesion, rendering Kras^V12 levels an integrator of micro-environmental signals that translate into cellular function. By live cell imaging of tumor models we observe shedding of mixed high and low Kras^V12 expressers forming multi-functional collectives with potentially optimal metastatic properties composed of a highly mobile and a highly tumorigenic unit.

Discussion—Together these data highlight previously unappreciated roles for the quantitative effects of expression level variation of oncogenic signaling molecules in conferring fundamental alterations in cell function regulation required for cancer progression.

Keywords

Cancer; Hypoxia; Kras; Motility; Adhesion

---

[*]To whom correspondence should be addressed: Gaudenz.Danuser@UTSouthwestern.edu.
[2]Current address: David H. Koch Institute for Integrative Cancer Research, Massachusetts Institute of Technology, Cambridge, Massachusetts 02139

Introduction

Kras belongs to the GTPase family of molecular switches that initiate several signaling cascades (Boettner and Van Aelst, 2002) such as the MAPK (mitogen-activated protein kinases) and the PI3-kinase pathways in response to growth factor receptor stimulation. Activation of these pathways leads to changes in gene transcription regulation (Roberts and Stinchcombe, 2013) as well as shifts in cytoskeletal dynamics (Malliri and Collard, 2003). In particular, extracellular signal-regulated kinase 1/2 (ERK) as part of the MAPK pathway can regulate Actin dynamics (Mendoza et al., 2011b, Mendoza et al., 2011a, Mendoza et al., 2015) or Myosin II activity (Klemke et al., 1997, Stupack et al., 2000) causing changes in cell motility and invasion. In many cancers Kras is associated with gain-of-function mutations (GOF) (Prior et al., 2012). Such mutations cause enhanced proliferation and survival leading to malignant tumorigenicity. They also contribute to a higher risk of metastasis (Pylayeva-Gupta et al., 2011). In the particular case of lung cancer, GOF mutations are generally related to a constitutively active form of the Kras protein (Scheffzek et al., 1997), which is thought to dramatically elevate the activation of downstream pathways independent of growth factor signaling (Schubbert et al., 2007). Among these mutations the glycine to valine mutation at codon 12 ($Kras^{V12}$) leads to enhanced metastatic potential and therefore is considered to be among the most lethal (Ihle et al., 2012).

Aberrant cell motility and dissemination is one characteristic of metastatic cancer cells and represents the most challenging problem in clinical cancer research. During this process cancer cells need to detach from the primary tumor, move through different extracellular environments and spread to distant sites. In order to metastasize efficiently, cancer cells switch between various modes of motility e.g. from amoeboid to mesenchymal or in some instances migrate collectively (Sanz-Moreno et al., 2008, Friedl, 2004, Friedl et al., 2012). Such morpho-dynamic plasticity provides the cancer cells with an enhanced capability of adaptation to different external environments (Sahai, 2005). This malignant cellular behavior influences the response to standard cancer therapies and therefore has strong clinical implications (Aparicio et al., 2015).

In addition to oncogenic changes and cellular plasticity, tumor hypoxia is also correlated with poor prognosis in lung cancer (Vaupel and Mayer, 2007). Hypoxia promotes stem-like characteristics of cancer cells, tumor growth, and dissemination (Axelson et al., 2005, Harris, 2002, Keith and Simon, 2007). It was also shown that hypoxia induces extracellular matrix (ECM) remodeling and thus affects the composition and organization of the tumor microenvironment (Gilkes et al., 2014). Biophysical and biological properties of the ECM directly regulate cellular motility and metastatic behavior (Lo et al., 2000, Levental et al., 2009), for example mediated by focal adhesion kinase (FAK) activation, which promotes tumor progression, metastasis, motility and drug resistance (Sulzmaier et al., 2014, Hirata et al., 2015). All together these previous studies indicate the importance of external signals in the regulation of cellular response and behavior.

In this study, we analyzed the effect of hypoxia and ECM stiffness on $Kras^{V12}$ protein levels in lung cancer morphogenesis. We found that $Kras^{V12}$ protein levels are substantially up-regulated upon long-term hypoxia. Such changes in $Kras^{V12}$ protein concentration control a

morpho-dynamic switch to sphere-like, tumorigenic and immobile cells. Upon adhesion initiation, $Kras^{V12}$ levels are down-regulated, which in turn induces adoption of a spreading and highly mobile phenotype. The switch between phenotypes is conferred by differential activation of a mechano-sensitive double-negative feedback between $Kras^{V12}$/ERK/Myosin II and matrix-adhesion signaling. Additionally, we found that clusters of cells with different $Kras^{V12}$ levels and thus different motile function can disseminate together as a multi-functional unit. With this we established that variations in the expression levels of a mutated oncogene, here $Kras^{V12}$, rather than harboring the mutation itself, regulate profound switches in cellular function and behavior.

Methods

Cell lines, cell culture, clonal separation, sphere and collagen assay

Human bronchial epithelial cells immortalized with Cdk4 and hTERT expression (HBEC) or immortalized HBEC transformed with p53 knock-down, $Kras^{V12}$ and cMyc expression ($HBEC^{p53-cMyc-Kras}$) (Sato et al., 2013) were cultured in keratinocyte serum-free medium (KSFM, Gibco) supplemented with 50 mg/ml of bovine pituitary extract (Gibco), 5 ng/ml of EGF (Gibco) and 1% Anti-Anti (Gibco) in a humidified incubator at 37°C, 5% CO_2 and 21% O_2 or at 2% or 1% O_2 in special hypoxia incubators (Nuaire) where O_2 is exchanged with N_2. For analysis of the effect of hypoxia (1–2% O_2), cell lines were cultured in long-term hypoxia which was defined as >4weeks. If not otherwise indicated, all experiments and cell culture was performed in 2% O_2. Only for normoxia (21% O_2) and hypoxia comparison, cells were cultured in 21% O_2. To induce sphere formation, $HBEC^{p53-cMyc-Kras}$ or clones were cultured in low attachment dishes (Corning) for 10–11 days before the experiments. For re-attachment, spheres were dispersed, seeded into plastic dishes and cultured for 10 days before imaging and lysis. For adherent and sphere-like cell population comparison in H2887 and $HBEC^{p53-cMyc-Kras}$, spheres that were mostly floating in the media were collected by spinning down the supernatant from cell culture in regular plastic dishes. Remaining attached cells from the same dish were lysed separately. Single clones were isolated from $HBEC^{p53-cMyc-Kras}$ by diluting the cell counts down to ~90 single cells total and spreading these cells throughout a 96-well plate. Wells with more than one clonal colony were dismissed. Clones were sub-cultured after reaching ~70% confluence and categorized as low or high $Kras^{V12}$ clone based on their $Kras^{V12}$ expression level analyzed by western blot. For the migration assay in collagen, bovine Collagen I (Advanced BioMatrix) was neutralized to pH: 7 and diluted 1:3.4 in KFSM. Afterwards, the mix was transferred into glass bottom dishes (LAB-TEK) and solidified for 1.5 h at 37°C which created a layer of ~720 μm thickness. $HBEC^{p53-cMyc-Kras}$ were seeded on top of the matrix in 1:3 diluted KSFM/PBS. Cells were imaged 2 days after seeding. The patient-derived lung cancer cell line H2887 and HCC4017 were provided by Prof. Minna (UT Southwestern Medical Center). These cells were cultured in RPMI 1640 medium (Gibco) supplemented with 5% cosmic calf serum (HyClone) and 1% Anti-Anti in a humidified incubator at 37°C, 5% CO_2 and 21%, 2% or 1% O_2. All cell lines were tested negative for Mycoplasma by using the Mycoplasma detection kit (Genlantis).

Cloning, virus production, infection and cell sorting

pLVX-GFP-Kras^{V12} vector was constructed by cloning a *SpeI/NotI*-digested Kras^{V12} fragments from pLenti-Kras^{V12}-vector (Vikis et al., 2007) into pLVX-IRES-Neomycin vector (Clontech). *EcoRI/SpeI*-digested GFP insert was ligated into the pLVX-IRES-Neomycin vector as *N*-terminal fusion protein. The virus was produced to the manufacturer's specifications. After collection of the virus, HBEC$^{p53-cMyc-Kras}$ cells were spin infected at 3000 rpm for 1 h at room temperature with the addition of 2 ug/ml Polybrene and briefly cultured in 21% O$_2$ to overcome hypoxia-induced reduction of infection efficiency. Transduced cells were then further cultured in 2% O$_2$ and selected with G418 (800 μg/ml, Gibco). Additionally, selected cells were sorted for GFP expression using a FACS Aria II sorter (BD Bioscience).

To down-regulate Kras^{V12}, pGIPZ shRNA against wild-type and mutated Kras (Oligo ID.: V2LHS_275818) from Dharmacon and a non-silencing shRNA (Dharmacon) was used as control. For virus production, HEK293FT cells were infected with 500 ng of shRNA against Kras, 200 ng of pMD2G and 300 ng psPAX2 using the transfection reagent Effectene (Qiagen) which was used according to manufacturer's protocol. Virus was collected starting 24 h after transfection in a 4:1 ratio of Dulbecco's modified Eagle's medium to Medium 199 containing 10% cosmic calf serum. HBEC$^{p53-cMyc-Kras}$ were treated with virus-containing media supplemented with 2 ug/ml Polybrene initially 1x for 5.5 h and 2x repetitively overnight. Afterwards, infected cells were selected with 3x repetitive overnight cycles using 10 ug/ml Puromycin diluted in KSFM. Subsequently, protein lysates were prepared and analyzed by western blot for total (wild-type and mutated) Kras down-regulation. Cells were imaged to determine change in morphology 6 days after selection.

Cell perturbations

High Kras^{V12} clones were treated with an initial dose of 20 nM of SCH772984 (Morris et al., 2013) (ChemieTek) for 48–68 h followed by 50 nM SCH772984 treatment for 24–48 h or with equivalent concentration of DMSO diluted in KSFM as control. After this treatment, samples were collected for western blot analysis. Live-cell imaging was started after increase to 50 nM SCH772984.

High Kras^{V12} clones were incubated with 500 nM blebbistatin (Sigma) or with equal concentration of DMSO in KFSM as control for 48 h. During this time, treatment was renewed every 24 h before samples were lysed for western blot analysis or cells were imaged documenting morphology changes. Live-cell imaging for migration analysis was started 43 h after treatment.

Low Kras^{V12} clones were treated with 50 μM FAK inhibitor 14 (Golubovskaya et al., 2008) (Tocris) or with equivalent concentration of DMSO diluted in KSFM as control for 48 and 72 h. After initial 24 h, treatment was renewed. Images were taken after 48 h and samples for western blot analysis were collected 48 and 72 h after treatment.

Low Kras^{V12} clones were cultured in 1 or 2 nM of CalyculinA (Sigma) or in equivalent concentration of DMSO diluted in KFSM as control for 12–48 h. Images were taken 48 h after treatment. Samples for western blot analysis were lysed 12–48 h after treatment.

Elastically supported surfaces (ESS) with a stiffness of 28, 15 and 1.5 kPa were purchased from Ibidi. Before usage, these surfaces were washed with PBS. ESS as well as plastic dishes were coated with 10 ug/ml BSA (bovine serum albumin, Sigma) or with 0.5% Gelatin for H2887 culture for 1 h at 37°C. Afterwards, low Kras^{V12} cells or H2887 were seeded in the center of the dishes and let adhere for minimally 3 h before filling up with medium. Live-cell imaging of low Kras^{V12} samples was started 24 h, samples for western blot analysis were collected 24–48 h and images were taken 48 h after seeding. H2887 were cultured 24 h before images were taken and samples were lysed for western blot analysis. Morphologies were analyzed by categorizing the cells as adherent or sphere-like using phase contrast images. Percentages of adherent versus sphere-like cells were quantified and the mean plus standard deviation for six images per condition was calculated.

Disc-patterned, ready-to-coat CYTOOchips (CYTOO) were coated with 5, 20, 100 or 200 μg/ml bovine Collagen I (Advanced BioMatrix) using a 4 well CYTOOchamber (CYTOO) for 2 h at room temperature. Afterwards, the wells were washed 4 times with PBS and high or low Kras^{V12} cells were seeded in a density of 50,000 cells per ml in a volume of 100 μl and let spread for 1 h at 37°C in 2% O_2. Cell morphologies were assessed by phase contrast imaging using a CO_2, O_2 and heat controlled microscope system. Different areas per condition were imaged and each individual experiment was repeated 3 times. Cell morphologies were quantified as described above. Here, 11 to 16 data points were analyzed.

Microscopy and live-cell imaging

All live-cell (except the 3D collagen migration assay), immunofluorescence (IF) as well as the soft-agar z-stack imaging were performed on an inverted phase contrast and fluorescence Eclipse Ti microscope (Nikon) equipped with perfect focus, motorized stage for parallel data acquisition, CO_2 control, heated and humidified air for long term live-cell imaging, O_2 control for hypoxia imaging, a Zyla sCMOS camera, SOLA solid state white-light excitation system and a motorized filter turret with filters for DAPI, FITC and Texas Red. Nikon Elements was used as image acquisition software. All live-cell imaging was performed in 2% O_2 cultivation. For imaging of soft-agar assay, a 4x Plan Fluor objective, for Myosin II IF a 60x Plan Apo VC oil objective and for live-cell imaging and for Kras IF the 10x or 20x Plan Fluor objectives were used.

A standard phase contrast cell culture microscope Eclipse TS100 (Nikon) using a 4x Plan Fluor or 10x Ph1 objective equipped with a fluorescence lamp (Lumencor), FITC filter sets, a camera (IMAGINGSOURCE) and the IC Capture software (IMAGINGSOURCE) was used to document cell morphologies as well as an inverted Axiovert 200M microscope (Zeiss) equipped with a AxioCam MRm camera (Zeiss) and Axiovision software (Zeiss) using a 10x or 20x Ph1 A-Plan objective.

A fully equipped Axioscop histology upright microscope (Zeiss) was used to image the histology staining. This system operates with an Axiocam HRc color digital camera (Zeiss) and Axiovision software for image acquisition. Images were acquired using a 5x, 10x or 20x objective in combination with the high resolution mode of 3900×3090 pixel of the camera.

The 3D collagen migration assay was imaged on an Eclipse Ti microscope (Nikon) equipped with perfect focus, motorized stage, a CoolSNAP HQ2 monochrome CCD camera (Photometrics) and a heating control. Imaging was performed with a 20x Plan Fluor objective. Since the microscope was not equipped with CO_2 control the media was supplemented during imaging with 10 mM HEPES. MetaMorph software was used to image the cells every 10 min.

Assessment of membrane localization of the GFPKras^{V12} construct, as well as high resolution imaging of the cellular morphology of highly GFPKras^{V12}-expressing cells were performed on a custom-built axially swept light sheet fluorescence microscope (Dean et al., 2015). GFPKras^{V12}-expressing cells were seeded on gelatin-coated glass coverslips and fixed. For morphology assessment, cells were additionally stained for Actin with 1:200 diluted PhalloidinAlexa594 (Invitrogen). 3D images were acquired with an isotropic pixel size of $160 \times 160 \times 160$ nm. 3D volume renderings were performed using Amira 6.0.0 (FEI) with image brightness and contrast enhanced. For Movie3, the 3D image was rotated using Matlab (Mathworks) to align the direction perpendicular to the coverslip with the z-direction of the image, and for Movie6 the two channels were made equally semi-transparent.

Migration analysis

Migration velocity analysis was performed as described earlier (Schafer et al., 2012). Randomly selected cells that show motility were manually tracked. Cells within spheres were not tracked due to the limitations of accuracy of this method. Only cells that were tracked over a minimum of 100 min were used for velocity analysis. Imaging frequency for all experiments was 10 min. For the low and high Kras^{V12} clone comparison, low Kras^{V12} clones were imaged for 6 h. Since high Kras^{V12} clones moved slower and to still get a correct measurement, clones were imaged over a period of 14 h. In total 2×50 cells each low Kras^{V12} clone and 39 or 50 cells each high Kras^{V12} clone were used for analysis. To compare the migration velocities in low Kras^{V12} clone expressing GFP or GFPKras^{V12}, cells were imaged for 6 h. For each condition 59 cells were analyzed. To study the effect of ERK inhibition on high Kras^{V12} cells, migration was analyzed over a period of 4 h for control and for treated cells. 50 control cell and 40 treated cells were analyzed. To investigate the effect of Myosin inhibition in high Kras^{V12} cells, migration of 74 control and 80 treated cells were analyzed over the period of 6 h. The same time course was used to study the migration changes of low Kras^{V12} cells seeded on plastic dishes or on 15 kPa or 1.5 kPa soft ESS. Here, 60 cells on plastic, 57 cells on 15 kPa ESS and 60 cells on 1.5 kPa ESS were analyzed.

To quantify the migration behavior, tracks from the analysis described above were used and individual cell trajectories were linear-smoothened over 3 time-points (total 30 min). This was done to account for eventual inaccuracies during tracking. If a track showed one or more zero displacements, the cell was categorized as interrupted moving. Cells without stopping (all displacement values >0) were categorized as persistent. To make the data sets from low and high Kras^{V12} clones comparable, only the first 6 h of high Kras^{V12} clones were used for this analysis. Numbers of cells analyzed are indicated in each figure legend.

Protein lysis and western blotting

Cells were washed once with ice-cold PBS on the plate or in terms of spheres, spun down, re-suspended in PBS and again spun down for further lysis. Cells were lysed in ice-cold lysis buffer (50 mM Tris, 2% SDS and 10% Glycerol) supplemented with Complete Protease and PhosSTOP Phosphatase inhibitor cocktail (Roche). Protein concentrations were measured using the BCA protein assay kit (Pierce). For western blot analysis, 4–30 ug of protein were diluted in Laemmli-buffer (Bio-Rad) and loaded per well. Proteins were separated on a 4–20% gel (Bio-Rad) in running buffer (Bio-Rad) and transferred on PVDF or Nitrocellulose (Thermo Scientific) membrane using wet transfer box (Bio-Rad). Membranes were blocked in 5% non-fat dry milk powder (MP) in PBS containing 0.1% Tween (PBST). Primary antibody incubation was done overnight at 4°C. The following antibodies and dilutions in 5% MP/PBST were used: 1:20,000 or 1:5,000 anti-beta-Actin (Sigma, AC-15), 1:100 anti-Kras (Santa Cruz, SC-30), 1:400 anti-p53 (Santa Cruz, DO-1), 1:500 anti-p44/42 MAPK (T202/Y204, pERK, Cell Signaling, E10), 1:1,000 anti-FAK (Cell Signaling, D2R2E), 1:500 anti-RasV12 (Cell Signaling, D2H12). The following antibodies were diluted in 5% BSA/PBST: 1:1,000 anti-cMyc (Cell Signaling, D84C12), 1:1,000 anti-ERK 1 (Santa Cruz, C-16), 1:500 anti-pFAK (Y397, Cell Signaling, D20B1), and 1:200 anti-Myosin light chain 2 (Cell Signaling, D18E2) and 1:100 anti-P-Myosin light chain 2 (T18/S19, Cell Signaling, 3674S) were diluted in 5% BSA/TBST (Tris-buffered solution containing 0.1% Tween). Before incubation, these membranes were washed 2x for 5 min with TBST. After incubation, membranes were washed 3x for 10 min in 5% MP/PBST and then incubated for 1 h with 1:2,000 HRP-tagged secondary antibodies against mouse or rabbit (Jackson ImmunoResearch) accordingly diluted in 5% MP/PBST. Membranes were developed using ECL reagent and imaged with G-Box (SynGene). To blot for Actin as standard (if not run separately), membranes were stripped with stripping buffer (0.08 M Tris/HCl, 2% SDS, 0.7 % β-Mercaptoethanol) at 50°C for 30 min and then re-blotted. Ratio analysis was performed using the software Gene Tools (SynGene) as well as the gel analysis tool from ImageJ (Wayne Rasband, NIH). Only samples run on the same membrane were compared.

Soft-agar assay and colony analysis

HBEC$^{p53-cMyc-Kras}$ were grown in 21% or in 2% O_2 for 5 weeks before analysis by the soft-agar assay. H2887 was cultured in 21% or in 1% O_2 for 8 weeks before putting into the soft-agar assay. In general, one bottom layer of 0.75% low-melting agar (Becton, Dickinson and Company) diluted in supplemented KSFM or RPMI 1640 was prepared in a 35-mm dish one day before cell seeding. To seed cells into the second layer, media/agar dilution was cooled down and kept at 42°C. 2,000 cells per dish were seeded. After the agar solidified, medium was added on top. Dependent on the pre-culture of the cells, the dishes were cultured in 21%, 2%, or 1% O_2 for 1 month. During this time the media was exchanged regularly. After 1 month, the colonies were fixed with 4% PFA (Electron Microscopy Sciences) in Dulbecco's PBS containing Ca^{2+} and Mg^{2+} (PBS, Sigma) for 1 h at 37°C. Afterwards, PFA solution was exchanged to PBS containing 30 mM Glycine (Sigma). Before imaging, colonies were stained with 1:500 Hoechst (Sigma) diluted in PBS for 1 h at 37°C followed by washing twice with PBS for 30 min. In a separate setup, big colonies from the HBEC$^{p53-cMyc-Kras}$ soft-agar assay were isolated and put back in culture for further experiments.

For colony analysis, the experiments for each condition were performed in three replicates. For each replicate 10 positions of the dish were imaged as z-stacks through the soft-agar layer. The field of view per each z-stack was 4160×3510 μm and the z-step was 50 μm. Custom Matlab software was designed to measure the number and size of colonies imaged by fluorescence microscopy. The program first discards non-circular, very small, and very large objects in each image. To find these objects the maximum intensity projection (MIP) of each z-stack over the axial (z) direction was used. Since the colonies are sparsely distributed it was assumed that they did not overlap laterally in the MIPs. Next, the MIPs were bandpassed with a lower frequency of ~5 μm (3 pixels) and a higher frequency of ~31 μm (19 pixels) (Crocker and Grier, 1996), and then a Rosin threshold was applied to the image. Since the colony shape is only apparent by including pixels that are below the Rosin threshold, the bandpassed images were thresholded at 10% of the Rosin threshold. Non-circular objects such as dust were excluded by discarding objects in the Rosin thresholded image that had circularity below 0.7 in the image thresholded at the lower intensity level. Circularity was defined as the area divided by the perimeter squared and normalized such that a circle would have a circularity of 1. In the Rosin thresholded image objects were discarded whose areas were too small (~21 μm^2) or too large (~4200 μm^2). Next, the positions of the colonies were identified. To find the lateral (x and y) positions of the colonies, the intensity peaks in the bandpassed MIPs were located. For each object in the Rosin thresholded image, its position was defined as the location of the intensity peak within the object with the highest associated intensity value in the bandpassed MIPs. To find the axial (z) positions of the colonies, a box around each x-y position was constructed with a width of 19 pixels in the lateral dimensions and encompassing the entire image in the axial dimension. The z-position of the associated colony was defined to be the z-position of the voxel in the box with the greatest intensity. When finding the lateral colony position, the image was first bandpassed. Finally, the diameter of the colonies was measured. First, the effective background was subtracted from the raw images. This was done by averaging each raw image across the z-dimension, blurring the averaged image with a Gaussian filter with a standard deviation of ~31 μm (19 pixels), and then subtracting the blurred image from every z-plane of the raw data. To reduce noise this background-subtracted image was blurred in the z-plane of the colony with a Gaussian filter of width ~1.5 μm (1 pixel). The blurred image was thresholded with a global threshold set by the user. The same threshold value was used for all colony radii measurements. As before, objects with circularity below 0.7 were removed as well as very small (~21 μm^2) and very large (4200 μm^2) objects. The diameter of the colonies was estimated as the square root of the area in the focal plane of the colony divided by π/2.

Immunofluorescence

For polarity assessment, high and low Kras^{V12} clones were seeded onto gelatin-coated glass cover slips. For Kras staining in sphere attachment assay, spheres were transferred on collagen I pre-coated plates (Corning) to induce attachment for 24 h. All samples were fixed at the end of the experiment with 4% PFA diluted in Dulbecco's PBS containing Ca^{2+} and Mg^{2+} (PBS) for 20 min at 37°C. Afterwards, samples were washed or stored until staining in 30 mM Glycine/PBS.

For staining of low and high Kras[V12] clones for Myosin II, phosphorylated Myosin and Actin, cells were blocked for 1 h at room temperature with 10% Goat serum in PBS containing 0.3% Triton. Primary antibody against Myosin IIa (BioLegend, #PRB-440P) or against phosphorylated Myosin (P-Myosin Light Chain 2, S19, Cell Signaling, 3671) was diluted 1:400 or 1:50 respectively in 1% BSA/PBS containing 0.3% Triton and incubated over night at 4°C in a humidified chamber. Afterwards, the samples were washed 3x for 5 min with PBS plus 0.2% Tween-20. Secondary antibody against mouse conjugated with Alexa488 (Invitrogen) was diluted 1:500 and mixed with 1:200 Phalloidin Alexa594 (Invitrogen) and 1:1000 Hoechst in 1% BSA/PBS containing 0.3% Triton and incubated for 1 h at 37°C. Finally, the samples were washed 3x for 5 min in PBS/0.2% Tween-20 and once in MilliQ before mounting with Fluoromount.

For the sphere attachment assay, cells were permeablized for 10 min in 0.2% Triton/PBS, then washed once in 10% Goat serum in PBS containing 0.2% Tween-20 and then blocked for 2 h at room temperature with 10% Goat serum/PBS/0.2% Tween-20. Primary Kras antibody (Santa Cruz, SC-30) was diluted 1:50 in 10% Goat serum/PBS/0.2% Tween-20 and incubated over night at 4°C in a humidified chamber. Afterwards, the samples were washed 3x for 10 min with 5% Goat serum/PBS plus 0.2% Tween-20. Secondary antibody against mouse conjugated with Alexa594 was diluted 1:200 and mixed with 1:1000 Hoechst and in 10% Goat serum/PBS/0.2% Tween-20 and incubated for 1 h at 37°C. Finally, the samples were washed 3x for 10 min in PBS/0.2% Tween-20 and once in PBS before imaging.

Flow Cytometry

H2887 cells were cultured in 2% O_2 over 4 weeks and fixed with 2% PFA in PBS for 20 min at 37°C. Afterwards cells were washed with 30 mM Glycine/PBS. Cells were permeablized for 2 min in 0.03% Triton/PBS, then washed once in PBS and blocked for 2 h at room temperature with 10% Goat serum in PBS. Primary Kras antibody (Abcam, ab55391) was diluted 1:50 in 10% Goat serum/PBS and incubated over night at 4°C in a humidified chamber. Afterwards, the samples were washed 3x for 10 min with 5% Goat serum/PBS plus 0.2% Tween-20. Secondary antibody against mouse conjugated with Alexa488 was diluted 1:500 in 10% Goat serum/PBS and incubated for 1 h at room temperature. Finally, the samples were washed 3x for 10 min in PBS/0.2% Tween-20 and once in PBS. Detached spheres were always collected by centrifugation and added back into the staining process. Finally, all cells were detached by Versene (Gibco) treatment and gentle scraping, collected, washed once and re-suspended for analysis in PBS. Kras intensities were analyzed using the BD FACS Aria II SORP (BD Biosciences) with a 488 nm excitation laser and a 530/30 band pass filter and gates were selected for viable cell population. Graphical analysis was performed using FlowJo v.10software (FLOWJO, LLC.).

Immunohistochemistry

Slides with paraffin-embedded human lung tumor tissue sections tested positive for Kras[V12] mutation were obtained from the *Cooperative Human Tissue Network* (CHTN) following UT Southwestern IRB approval (IRB#: STU 102014-009). A 1:200 dilution of anti-Kras antibody (Abcam, ab55391) and a 1:80 dilution of Hif1α antibody (Novus, NB100-105) were used to stain for Kras[V12] and Hif1α, respectively. 1:50 dilution of pERK (T202/Y204,

pERK, Cell Signaling, E10), 1:50 dilution of pFAK (Y397, Cell Signaling, D20B1) and 1:100 dilution of pMLC (T18/S19, Cell Signaling, 3674S) were used. To compare $Kras^{V12}$, Hif1α, pERK, pFAK and pMLC overlay, sequential slides were stained for Kras following Hif1α, pERK, pFAK and pMLC in the next consecutive sections. The Vectastain protocol provided for the Vectastain Elite PK-6102 kit (Vector Laboratories) was used for all immunohistochemistry experiments. Briefly, slides were heated at 57°C for 15 min and de-paraffinized by washing three times in Xylene for 5 min. Slides were then incubated in 100% Ethanol for 5 min followed sequentially by 2 min washes in 90%, 80%, 70%, and 50% Ethanol. Subsequently, slides were placed in water for 5 min to complete rehydration. Slides were then placed in sodium citrate (0.01 M sodium citrate dihydrate, 0.05% Tween, pH: 6.0) and boiled for 3 min for antigen presentation. Afterwards, slides were washed in water and equilibrated in TBST (0.02 M Tris, 0.1% Tween, 0.15 M NaCl, pH: 7.6). Endogenous peroxidase was blocked by incubating the slides in 0.3% H_2O_2 for 30 min. Slides were washed twice for 5 min in the TBST. Endogenous Biotin and Avidin were blocked using a Biotin/Avidin blocking kit (SP-2001, Vector Laboratories). Tissue sections were then blocked with horse serum for 1 h. Sections were treated overnight at 4°C with primary antibody prepared in blocking solution at dilutions described above. A high salt wash was performed twice for 5 min in TBST containing 0.3 M NaCl. Slides were treated with anti-mouse secondary antibody (provided by Vectastain Elite PK-6102 kit) diluted 1:200 in blocking solution for 30 min at room temperature. Slides were washed twice with TBST and treated with the Vectastain reagent for 30 min. Following 2×5 min washes in TBST, slides were developed by adding peroxidase substrate (ImmPACT DAB Peroxidase Substrate Kit, SK-4105, Vector Laboratories) and were observed immediately under a light microscope. The reaction was stopped by washing slides in water, and the time for development was kept consistent for all slides. Hematoxylin staining was performed once the slides were dry by incubating slides in Hematoxylin for 15 sec, followed by 2x washes with TBST and a final wash in water. Following drying, slides were covered with a cover-slip for imaging.

Nuclei aspect ratio measurements

Images of areas with low and high $Kras^{V12}$ staining with lung tumor section from 5 patients were acquired and nuclei shape was assessed using ImageJ. Areas were assigned visually by intensity of brown Kras staining. No brown staining was defined as low $Kras^{V12}$ and clear, strong brown signal was defined as high $Kras^{V12}$ areas. The nuclei stained with Hematoxylin were outlined manually and the aspect ratios of the nuclei of all cells within the defined areas were measured in ImageJ. The following numbers of nuclei were analyzed for each patient: Patient1: low $Kras^{V12}$: 587, high $Kras^{V12}$: 172; Patient2: low $Kras^{V12}$: 420, high $Kras^{V12}$: 189; Patient3: low $Kras^{V12}$: 222, high $Kras^{V12}$: 131; Patient4: low $Kras^{V12}$: 274, high $Kras^{V12}$: 110; Patient5: low $Kras^{V12}$: 283, high $Kras^{V12}$: 87.

RNA isolation and KRAS droplet digital reverse transcription (RT) PCR

To analyze the levels of total (wild-type and mutated) KRAS mRNA changes upon long-term hypoxia culture in $HBEC^{p53-cMyc-Kras}$ and H2887, we utilized droplet digital RT PCR (ddPCR). Cells were grown for 6 weeks in 21 or 1% O_2. Afterwards, RNA was isolated from 5 independent repetition samples for each condition using the High Pure RNA

Isolation Kit (Roche). RNA concentration was measured using the Synergy system (BioTek). Up-regulation on the protein level of Kras^{V12} was confirmed by western blot before ddPCR analysis. RNA was reverse transcribed (100 ng input) into first strand cDNA with iscript (Bio-Rad) in the presence of an exogenous spike-in control RNA for RT efficiency correction (bacteriophage MS2 RNA; Roche). Following cDNA synthesis, cDNAs were diluted 1:4 and 2 μl of diluted cDNA was mixed with a reaction containing primers and 5′ hydrolysis probes for both KRAS (F-5′-tggacgaatatgatccaacaat, R-5′-tccctcattgcactgtactcc; Universal Probe library #62-6FAM, Roche) and MS2 viral genes for assembly protein 1 (F-5′-GTCGCGGTAATTGGCGC, R-5′-GGCCACGTGTTTTGATCGA, probe-5′-HEX-AGGCGCTCCGCTACCTTGCCCT-bhq1) and the lysis protein (F-5′-CCTCAGCAATCGCAGCAAA, R-5′-GGAAGATCAATACATAAAGAGTTGAACTTC, probe-5′-HEX-CAAACATGAGGATTACCCATGTCGAAGACA-bhq1). Following droplet generation, PCR was performed with the following thermoprofile (95°C for 10 min for polymerase activation, 40 cycles of 94°C for 30 sec, 60°C for 1 min, 98°C for 1 min for polymerase inactivation and 20°C hold). Droplets were then read in a flow-cytometer like fashion and scored for absence or presence of fluorescence. Following correction of molecule counts for multiple templates per droplet (Poisson distribution correction) molecule per microliter counts are obtained for KRAS transcripts and exogenous MS2 assembly and lysis transcripts. To correct for RT efficiency differences between samples molecule counts were normalized to the average of both MS2 transcript levels. Following normalization to MS2, total molecule numbers were calculated by multiplying the molecules per microliter data by 20 (20 μl PCR volume). These data were expressed as molecules of KRAS RNA per 10 ng of input RNA.

Statistical analysis

Data representation was done using Excel (Microsoft). The Kolmogorov-Smirnov-test was used to test data sets for normality. This was done using the Prism6 software (GraphPad). If failed an unpaired, two-tailed Mann-Whitney test was applied as indicated in figure legends; otherwise, a two-sided, unpaired Student's t-test was applied to determine the significance of differences between two data sets. For the comparison of multiple data sets a one-way, multi-comparison ANOVA-test was used. A P-value of <0.05 was assigned as significantly different and P-value of <0.05 was indicated as *, of <0.01 as ** and of <0.001 as *** in the figures.

Results

Long-term hypoxia promotes sphere-like morphology and increases Kras^{V12} protein levels *in vitro* and *in vivo*

We first examined the effect of long-term hypoxia in an isogenic cell model of metastatic lung cancer, which had been derived from normal, immortalized (with hTERT and cdk4) human bronchial epithelial cells (HBEC) and transformed by knock-down of p53, and ectopic expression of cMyc and Kras^{V12} (HBEC$^{p53-cMyc-Kras}$). Under atmospheric (~21% O_2) conditions these cells are morphologically heterogeneous (Sato et al., 2013) (figure 1(a), left). Upon long-term, hypoxic cultivation (>4weeks in 2% O_2), we found that

HBEC$^{p53\text{-}cMyc\text{-}Kras}$ increasingly homogenized and assembled in sphere-like clusters (figure 1(a), right). This change was accompanied by an increase in Kras^{V12} protein expression levels (figure 1(b)). No cell death was observed due to long-term low Oxygen culture conditions. Careful separation of sphere-like clusters from adherent, spread cells within the same culture revealed that spheres exhibited higher Kras^{V12} expression (figure 1(c)). In addition, knock-down of Kras (wild-type and mutated) in HBEC$^{p53\text{-}cMyc\text{-}Kras}$ abrogated the sphere-like phenotype (figure 1(d), (e)). The same morphological changes (figure 1(f)), as well as an increase in Kras^{V12} expression (figure 1(g)), specifically in the spheres (figure 1(h)), was observed under long-term hypoxic culture in the patient-derived non-small cell lung carcinoma cell line H2887 harboring the Kras^{V12} mutation. Untransformed HBECs bearing wild-type Kras did not show changes in either morphology (figure 1(i)) or Kras expression (figure 1(j)) under hypoxic conditions, assigning this effect specifically to mutated Kras-transformed cancer cells. Upregulation of the mutated Kras^{V12} in HBEC$^{p53\text{-}cMyc\text{-}Kras}$ upon hypoxia was confirmed using a mutation-specific antibody (figure 2(a)). Direct comparison of total Kras (wild type and mutated) and only mutated Kras^{V12} protein levels determined Kras^{V12} being upregulated to hypoxia. Together, these data suggest a correlation between hypoxia, Kras^{V12} expression, and cell morphology. To further characterize the hypoxia-driven increase in Kras^{V12} expression, we first confirmed that short-term (24–48 h) exposure to low Oxygen did not lead to increased Kras^{V12} protein levels in HBEC$^{p53\text{-}cMyc\text{-}Kras}$ and H2887 cells (figure 2(b)). Direct comparison of the effect of hypoxia on Kras^{V12} protein (supplementary figure 1(a)) and on mRNA levels in HBEC$^{p53\text{-}cMyc\text{-}Kras}$ as well as in H2887 harboring intrinsic Kras^{V12} mutation (supplementary figure 1(b)) revealed that the up-regulation in both cell lines is controlled at the protein level suggesting interference between hypoxia and translation of Kras^{V12} protein recycling- and/or degradation. Importantly, neither cMyc nor p53 levels changed in HBEC$^{p53\text{-}cMyc\text{-}Kras}$ upon long-term 2% O_2 culture in both cell lines, excluding a role of cMyc nor p53 protein levels in the observed morphology changes (supplementary figure 1(c), (d)). Since expression of the oncogenic form of Kras is related to increased tumorigenic potential (Pylayeva-Gupta et al., 2011), we also performed soft-agar colony formation assays with HBEC$^{p53\text{-}cMyc\text{-}Kras}$ and H2887 cells (figure 2(c), (g)) to test whether hypoxia-induced Kras^{V12} up-regulation promotes tumorigenicity. Indeed, both cell lines showed an increase in the number (figure 2(d), (h)) and size (figure 2(e), (i)) of the colonies under low Oxygen conditions. The increase went along with increase in Kras^{V12} expression levels in the colonies (figure 2(f)), indicating a central role of Kras^{V12} protein concentration for *in vitro* tumorigenicity.

Our *in vitro* data provide strong evidence that Kras^{V12} expression levels are sensitive to long-term hypoxia and that such increase in Kras^{V12} can trigger a profound switch in cell morphogenesis. We next tested if this may also apply *in vivo*. For this purpose, lung tumor sections from 5 patients tested positive for Kras^{V12} were stained for Kras. All sections displayed a heterogeneous Kras^{V12} expression pattern with hotspots of high Kras^{V12} expression levels throughout the tumor (figure 2(j)). To test whether these hotspots correlate with hypoxic areas in the tumor mass we stained sequential tumor sections for Kras or for Hif1α, which is a marker for hypoxic areas (figure 2(k)). Indeed, we found that neighbor tumor sections showed same areas positive for Kras^{V12} and Hif1α expression in all 5

patients (figure 2(k), (j) and supplementary figure 1(e)). We further wanted to test if this localized coupling of Kras^{V12} expression and hypoxia would be associated with morphological changes akin to those observed with high Kras^{V12} expression *in vitro.* For these analyses, areas of low and high Kras^{V12} staining within the same tumor were identified (supplementary figure 2(a)–(c)) and the aspect ratio (ratio between the long and short axes of an ellipse approximating the nuclear outline) of the nuclei (supplementary figure 2(d)) was used as a proxy for cellular morphology (Irshad et al., 2014, Sanchez-Laorden et al., 2014). Regions with high or low Kras^{V12} staining displayed a significant difference in nuclear shape: the former contain round nuclei (aspect ratio ~1), the latter contain elongated nuclei (aspect ratio ≫1) (supplementary figure 2(e), (f)). Together, these histological analyses support the correlation between hypoxia, Kras^{V12} protein levels and cell morphogenesis. All the following experiments were conducted under hypoxic conditions.

Differential Kras^{V12} protein levels are associated with clonal morphology and migration behavior

First, we investigated the mechanism by which differential expression levels of constitutively active Kras^{V12} signal translate into different cell morphological programs. We isolated single clones from HBEC$^{p53-cMyc-Kras}$ in 2% O_2 culture conditions and obtained stable clones with an adherent, spread morphology and similarly stable clones with a predominant sphere-like, non-adherent morphology (figure 3(a)). These morphologically selected clones differed vastly in Kras expression (figure 3(b)). Knock-down of Kras in HBEC$^{p53-cMyc-Kras}$ led to a reduction in the sphere-like phenotype (figure 1(d), (e)). Comparison of Western blots using generic versus mutation-specific Kras recognizing antibodies confirmed the involvement of the mutant form in the sphere-like clones (figure 3(c)). The mutant-specific antibody was tested in different lung cancer cell lines bearing different Kras mutations to determine background and specificity of the antibody (supplementary figure 3(a)). No signal was detected in cell lines negative for the Kras^{V12} mutation confirming the presence of Kras^{V12} protein in the low Kras^{V12} clones. Moreover, no differences in cMyc expression were observed between the clones, supporting a specific association between Kras^{V12} expression and the observed morphological changes (supplementary figure 3(b)). Clonal separation of untransformed HBECs harboring only wild-type Kras neither produced morphological heterogeneity (figure 3(d)) nor showed variation in Kras protein levels (figure 3(e)). This underlines the dependence of the morphological switches in HBECs on a transformation with oncogenic Kras^{V12}.

To analyze the migration behavior of HBEC$^{p53-cMyc-Kras}$ clones, we imaged and tracked random, single cell migration over the time course of 6 h under 2% O_2 conditions. Low Kras^{V12} clones migrated with a mean velocity between 1.3 and 1.6 µm/min (figure 3(f)). The movement was persistent (figure 3(g), only 1 out of 50 cells intermittently stopped migration, supplementary figure 3(c), Movie1). High Kras^{V12} clones grew mostly in sphere-like clusters with little observable movement. However, when cultured for longer they began to shed cells that subsequently adhered to the surface and initiated motility (Movie2). Even though these cells formed adhesions and started to migrate and thus likely differed from cells inside clusters in terms of Kras^{V12} levels, they showed markedly reduced motility compared to low Kras^{V12} clones, both in mean velocity and persistence (figure 3(f), (h); 38

out of 39 tracked cells showed an interrupted movement with at least one complete stop throughout the observation window; supplementary figure 3(c), Movie2). From this we conclude that low and high $Kras^{V12}$ clones differ in their activation of the cell motility machinery and their ability to maintain stable polarity.

We next tested if motile low $Kras^{V12}$ clones could be converted into sphere-forming, non-motile cells by ectopically inducing high $Kras^{V12}$ levels. Low $Kras^{V12}$ clones in 2% O_2 culture conditions were stably infected with either a CMV-driven $GFPKras^{V12}$ to accomplish high $Kras^{V12}$ levels or an empty control GFP vector. Membrane localization of the $GFPKras^{V12}$ construct was confirmed by 3D light sheet fluorescence microscopy (Movie3). Introduction of high levels of $Kras^{V12}$ expression into low $Kras^{V12}$ clones fully recapitulated the phenotype observed in high $Kras^{V12}$ clones (figure 3, Movie4, 5). $GFPKras^{V12}$-expressing cells adopted a sphere-like morphology (figure 3(i), Movie6) and their mean migration velocity was significantly reduced (figure 3(j)) along with a decrease in migration persistence (figure 3(k), (l)) (increase of interrupted trajectories from 2% to 18%, 11 out of 60 cells, supplementary figure 3(d)). These data corroborate the roles of $Kras^{V12}$ expression levels in cell morphology and motility control.

$Kras^{V12}$ expression differentially activates a FAK/ERK/Myosin signaling

Next, we asked which signaling pathways could translate $Kras^{V12}$ expression levels to differential morphology. Since the two phenotypes showed differences in adhesive properties we first tested the coupling of $Kras^{V12}$ expression levels and cell adherence. We cultured $HBEC^{p53-cMyc-Kras}$ either in adherent or in low attachment cell culture dishes in 2% O_2 culture conditions. Low attachment plates initiated an exclusively sphere-like morphology of the cell line accompanied by increased $Kras^{V12}$ levels (figure 4(a)). As expected (Mitra et al., 2005), FAK activity in high $Kras^{V12}$-expressing spheres on low attachment dishes was much reduced, as seen in a decrease in FAK phosphorylation (figure 4(a)). Moreover, Kras is upstream of ERK activity (Rajalingam et al., 2007), which is a potential regulator of cell morphology through its capacity of activating Myosin II (Brahmbhatt and Klemke, 2003). High Myosin activity could promote a round, sphere-like phenotype (Lomakin et al., 2015). Therefore, we analyzed both ERK and Myosin II activation and indeed found both upregulated in high $Kras^{V12}$ spheres (figure 4(a)). Based on these data we envisioned a pathway where adhesion signaling modulates the concentration of constitutively active $Kras^{V12}$, which in turn controls the level of ERK and Myosin activity (figure 4(b)). Differential activation between adherent and sphere-like cells was confirmed in the patient-derived lung cancer cell line H2887 (supplementary figure 3(e)). Moreover, staining for pERK, pMLC and pFAK in human lung tumor sections support the notion of a differential activation of the proposed pathway in high versus low $Kras^{V12}$–expressing tumor areas (figure 4(c)). pERK as well as pMLC were both activated heterogeneously throughout the tumor similarly to the observed $Kras^{V12}$ distribution whereas pFAK staining was low. The staining was performed on consecutive sections. Therefore, a direct overlay of the signal was not expected.

Kras^{V12} levels associate with a switch in FAK/ERK/Myosin II activation

Our migration analysis showed big differences in the ability to maintain persistent movement in low versus to high Kras^{V12} clones (figure 3(g, h), supplementary figure 3(c)). The lack of polarity with one clearly defined lamellipodium could cause the reduced average velocity and persistence of single cell motility in these clones. Low Kras^{V12} clones with reduced ERK and Myosin II activity displayed robust separation of a well-defined actin-rich lamellipodia at the cell front and an actomyosin-rich rear, whereas high Kras^{V12} clones with high ERK and Myosin II activity lacked clear asymmetry in Myosin distribution and displayed multiple sites of cryptic lamellipodia (figure 4(d)). Similar distributions were also observed with staining for phosphorylated Myosin (figure 4(e)). Based on this data we expected that the morphological switches from high to low Kras^{V12} expression could be reproduced by direct inhibition of Myosin II or ERK. To test this, we first treated high Kras^{V12}, sphere-like clones with the specific ERK inhibitor SCH772984 (Morris et al., 2013). This resulted in a decrease in ERK phosphorylation (figure 5(a)) which was comparable with the activation levels observed in the adherent, motile phenotype (compare figure 4(a)). In support of our hypothesis, this treatment led to a striking conversion of sphere-like into adherent cell morphology (figure 5(b)), accompanied by significantly faster (figure 5(c)) and more persistent movements (figure 5(d), 85% up from 8% of cells moved persistently after ERK inhibition, supplementary figure 3(f), Movie7, 8). At the same time activation of adhesion signaling as measured by FAK phosphorylation was observed (figure 5(a)), consistent with the notion that motile cells display increased mechanical engagement of integrin-mediated matrix adhesions. Most critically, we found that Kras^{V12} levels significantly decreased in these cells (figure 5(e)). Thus, inhibition of ERK reduced the expression level of the mutated Kras^{V12} protein presumably dependent upon adhesion engagement. To test directly the existence of a mechano-transductory feedback we disrupted adhesion signaling by selective inhibition of FAK using the small molecule compound FAK inhibitor 14 (Tocris). This treatment resulted in decreased FAK phosphorylation (figure 5(f)) comparable with the decrease observed in the sphere-like phenotype (compare figure 4(a)) and led to conversion of adherent clones into cells with a sphere-like morphology (figure 5(h)) and elevated Kras^{V12} expression (figure 5(i)). Along with this switch, ERK signaling was activated (figure 5(g)). Altogether, these data put Kras^{V12} expression levels into a double-negative feedback loop, in which ERK activation downstream of high concentrations of constitutively active Kras^{V12} promotes Myosin II activity that blocks cellular polarization and cell adhesion. Upon decrease of either Kras^{V12} concentration or ERK signaling, cells can spread and induce adhesion signals that reduce Kras^{V12} concentration further by a yet to be determined mechanism.

Next, we tested whether we could control Kras^{V12} levels and associated FAK/ERK switches by increasing and decreasing Myosin activity. We first reduced Myosin II activity in high Kras^{V12} clones by applying the Myosin II-specific ATPase inhibitor blebbistatin. This led to the formation of more adherent, spread cells (figure 6(a)) with significantly increased migration velocity (figure 6(b)) and persistence (figure 6(c), increase from 4% to 69% cells with persistent motion, supplementary figure 3(g), Movie9, 10). Importantly, decrease in Myosin II activity reduced the Kras^{V12} concentration levels (figure 6(d)) and ERK activation (figure 6(e)) whereas FAK phosphorylation was unaffected (figure 6(f)). Reduction of ERK

was also in the same range as already detected before in the adherent phenotype (figure 4(a)). Complementary, activation of Myosin II by treatments of adherent, low Kras^{V12} clones using CalyculinA (CalA), switched the cells to a sphere-like phenotype (supplementary figure 3(h)) without significant reduction in FAK activity (supplementary figure 3(j)), but significantly increased Kras^{V12} levels (supplementary figure 3(i)) and ERK phosphorylation (supplementary figure 3(k)). The CalA experiments may be difficult to interpret by themselves since CalA is not a specific Myosin activator; nonetheless, the consistency of the results with the blebbistatin experiments is noteworthy. Together these data support the double-negative feedback model in which the two cell morphologies and Kras^{V12} levels could be interconverted by manipulation of ERK, Myosin II or FAK.

Kras^{V12} levels respond to changes in the mechanical properties of the micro-environment

Another way to potentially interfere with adhesion engagement is by alteration of the mechanical micro-environment (Charras and Sahai, 2014). It is well established that adhesion engagement is more effective on stiff compared to soft substrates (Chan and Odde, 2008). Indeed, ECM remodeling within the tumor and its surroundings is a clinical hallmark of cancer progression (Hanahan and Weinberg, 2011); and ECM alignment and stiffness increase correlate with more efficient metastasis and tumor progression (Acerbi et al., 2015, Levental et al., 2009). To investigate the putative connection between mechano-transduction and Kras^{V12} expression, we first seeded low Kras^{V12} clones on elastically supported surfaces with decreasing stiffness (28, 15 or 1.5 kPa, representing a stiffness range of tissue and matrix *in vivo* (Discher et al., 2005)), where we observed less adhesion engagement than on infinitely stiff cell culture plastic (supplementary figure 4(b)). With decreasing substrate stiffness these low Kras^{V12} clones formed round, sphere-like clusters (figure 7(a), supplementary figure 4(a)). The remaining unclustered cell population appeared smaller and exhibited markedly lower mean migrating velocity (figure 7(b), Movie11–13). Population-wide analysis of the signaling state in this mixed culture showed that the lower mechanical engagement of adhesions led to a significant decrease in FAK phosphorylation (supplementary figure 4(b)), which was sufficient to increase Kras^{V12} expression levels on 15 and 1.5 kPa stiff surfaces and modest ERK activation (figure 7(c), supplementary figure 4(c)). On surfaces with a stiffness of 28 kPa no increase in Kras^{V12} was observed (supplementary figure 4 (d)). These findings were confirmed using the H2887 cell line where the switch in signaling and Kras^{V12} levels is even more pronounced (supplementary figure 4(e) – (g)). Cell morphology, FAK and ERK signaling as well as Kras^{V12} levels were all changed on softer substrates. We also performed the reverse experiment: High Kras^{V12} levels were initiated by culture of HBEC$^{p53-cMyc-Kras}$ in low attachment dishes followed by transfer of sphere-like clusters onto plastic dishes. This induced cellular morphology changes from exclusively sphere-like to mostly adherent populations (figure 7(d)) accompanied by a strong decrease in Kras^{V12} levels (figure 7(e)). To more directly test the effect of different ECM densities on cell morphologies in low compared to high Kras^{V12} clones, we seeded such clones on micro-patterned chips that prevented cluster formation and were coated with different Collagen I concentrations (5–200 μg/ml). After 1 h of spreading (supplementary figure 4(h)), low Kras^{V12}-expressing clones gave rise to a higher proportion of adherent cells compared to high Kras^{V12}-expressing clones, which showed significantly more sphere-like cells for all Collagen I concentrations (supplementary figure 4(i)).

Altogether, these manipulations support the notion of Kras^{V12} expression levels being controlled by an adhesion-dependent, mechano-sensitive switch.

Finally, we wondered whether the separation of cells in two discrete morphological states associated with and low and high Kras^{V12} expression would also occur with a population of patient-derived H2887 cells (supplementary figure 4(j)). To test this, H2887 cells grown under 2% O_2 conditions on adherent plastic dishes were fixed and stained for their intrinsic Kras^{V12} levels without interfering with their adhesion state. Kras^{V12} expression levels were then measured by flow cytometry. We found two separable populations with high and low Kras^{V12} levels (supplementary figure 4(j)). In addition, we consistently observed a small third population of cells with very high Kras^{V12} expression. In sum, these analyses showed that high and low Kras^{V12} expression is driven by the degree of mechano-transduction through cell-matrix adhesions.

Clusters of cells with high and low Kras^{V12} levels migrate together as a multi-functional unit

Live cell imaging of cell dissemination from high Kras^{V12} spheres showed a conversion to low Kras^{V12}, adherent and motile cell populations within a 23 h time period that resulted in cells leaving the sphere (figure 7(f), (g), Movie14). Curiously, we frequently observed small cell collectives, where one motile low Kras^{V12} expressing cell drags along one or several round, high Kras^{V12}-expressing cells (figure 7(f), (g), arrows, Movie14, 15). Such collectives of motile, spread and sphere-like cells were unveiled also by live cell imaging in a 3D Collagen environment (figure 7(h), Movie16). Interestingly, in this experiment we were able to observe the two cellular states, here purely judged on cell morphology and motility, in a 3D migration assay.

Discussion

Our data show that the concentration of a constitutively active signal, here of the oncogene Kras^{V12} can modulate divergent cell functions, allowing tumor cells to adopt plastic behavior (supplementary figure 5). We demonstrate that low levels of Kras^{V12} initiate an adherent and motile phenotype whereas high levels of Kras^{V12} protein induce a sphere-like, tumorigenic cell phenotype. Similar changes in morphogenesis were previously observed by introducing Kras^{V12} into normal fibroblasts (Guerrero et al., 2000), where it was concluded that the oncogenic versus the wild-type form of Kras is sufficient to induce a sphere-like morphology. Here, we show that the variation in expression level of the constitutively active Kras^{V12} mutation is sufficient to drive shifts in cell morphology rather than the mutation status alone. Our work adds to a large body of literature describing the effect of oncogenic Ras transformation on signaling and motility (Sahai et al., 2001, Lee and Helfman, 2004, Pawlak and Helfman, 2002). However, the past studies have compared the effect of wild-type versus mutated protein. Here, we show in a lung cancer model the relevance for differential expression of the mutated protein. We were able to dissect the signaling pathway in two independent cellular *in vitro* model systems. We could also show that such signaling is differentially activated in human lung tumor sections indicating the clinical relevance of our findings.

We show that Kras^{V12} protein levels respond to prototypical environmental cues in malignant solid tumors such as hypoxia and ECM stiffness. Under low Oxygen conditions, Kras^{V12} levels increase overall, driving a tumorigenic program of sphere-like, non-adherent cells (supplementary figure 5). In contact with an increasingly stiffer environment Kras^{V12} levels are suppressed, triggering the self-polarization and spreading of highly motile cells. Our data showed that low Kras^{V12} cells gain gradually a more sphere-like morphology on softer substrates with a range of 28, 15 or 1.5 kPa (supplementary figure 4 (a)). Kras^{V12} levels get increased on soft substrates with a stiffness of 15 or 1.5 kPa but not on 28 kPa stiff surfaces (figure 7 (c), supplementary figure 4 (d)). This data could indicate a threshold between 28 and 15 kPa for the mechano-sensitive response in Kras^{V12} protein levels. Much additional work will be required to define the exact mechanical conditions and mechanisms for this expression switch. Similarly, the link between hypoxia and Kras^{V12} protein levels remains to be discovered. Here, we focused on the pathway that relates Kras^{V12}, expression to a morphological switch between a sphere-like, immotile and a spread, motile cell phenotype. Our data establish that the switch is conferred by a mechano-sensitive double-negative feedback between Kras^{V12} expression and FAK/ERK/Myosin II activation (supplementary figure 5). Interference with the pathway at any level led to a conversion of the cellular state in terms of Kras^{V12} expression, signaling, and the morphology and motility features. Reduction in ERK as well as Myosin II activity induced an adherent and motile phenotype with reduced Kras^{V12} levels and FAK activation. Consistent with this, reduction of FAK phosphorylation switched the phenotype from adherent to a sphere-like morphology with high Kras^{V12} levels and increased ERK activity. Complementary to these findings, ECM stiffness modulation led to the same changes with increased Kras^{V12} levels and ERK activity, sphere-like morphology and reduced FAK activation. All these data demonstrate the robustness and consistency of the pathway. Critically, at this point we have no reasons to believe that the observed morphological switch represents a transition between an amoeboid and a mesenchymal state as described, for example, for melanoma and fibrosarcoma cell lines (Sanz-Moreno et al., 2008, Wolf et al., 2003). Amoeboid cells lack adhesion engagement. In our cell models, however, sphere-like cells can engage with the ECM both in 2D and 3D. We also have no evidence that the sphere-like cell state develops a low-adhesion mode of motility in constrained 3D environments as is typical for amoeboid cells (Liu et al., 2015). Therefore, given our results of a direct relation between Kras^{V12} levels and Myosin II activity, we rather suggest that the observed switch in morphology and motility relates to epithelial cell states with high and low contractility, as described for both 2D and 3D scenarios in (Lomakin et al., 2015). Indeed, we were able to trigger conversion between the sphere-like and spread cell state by down- and up-regulation of Myosin II activity.

In support of our proposal of a switch-like behavior of the pathway, we were able to identify mainly two populations with distinct morphologies and Kras^{V12} levels, first by mechanical separation from the same culture (figure 1(c), (h)) and second by isolation of stable clones (figure 3(a)–(c)). Moreover, by flow cytometry of a heterogeneous population of patient-derived lung cancer cells harboring intrinsically the Kras^{V12} mutation we found a separation between low and high Kras^{V12}-expressing cells, and a small population of very high Kras^{V12} cells (supplementary figure 4(h)). Previous studies found Kras associated in a complex together with unligated integrins located within the plasma membrane driving

tumorigenicity (Seguin et al., 2014). Our studies suggest that upon adhesion engagement as measured by FAK activation Kras^{V12} gets down-regulated. Together, these two studies put Kras within a pathway where adhesions can drive changes in Kras signaling and thus regulate malignant cellular behavior. The observed switch-like transition occurs over a period of less than 24 h. Of note, this time scale matches the time scale of Kras^{V12} protein half-life (Shukla et al., 2014), suggesting that protein degradation may be the rate-limiting factor in transitioning between the two cellular states and leading us to speculate that the regulatory effectors downstream of hypoxia and adhesion stimuli converge onto proteolytic pathways. We cannot completely exclude the possibility that the hypoxia-induced upregulation of Kras^{V12} could also be driven by a clonal selection. However, the upregulation of Kras^{V12} in a low attachment environment as well as the reverse downregulation by induction of attachment both occur on a time scale of hours or days, which seems to rule out a clonal selection mechanism. Future work will be necessary to unravel the potentially very complex relations between hypoxia, adhesion signaling and Kras^{V12}.

Our findings also present evidence that the Kras^{V12}-expression switch facilitates the formation of cell collectives composed of a highly mobile and a highly tumorigenic unit, in which highly mobile cells can efficiently disseminate highly tumorigenic cells. At this point we can only speculate that the two states are driven by adhesion signaling and differences in Myosin II activity in a 3D environment. Yet, it is intriguing to note recent reports that show invasive cell clusters and multi-cellular aggregates of circulating tumor cells correlate with the worst outcome for cancer patients (Aceto et al., 2014). Our *in vitro* experiments provide a new potential mechanism of how such clusters can form in Kras^{V12} mutated cancers. More detailed analysis needs to be performed in future studies to dissect the nature and role of such collective clusters.

Supplementary Material

Refer to Web version on PubMed Central for supplementary material.

Acknowledgments

References

ACERBI I, CASSEREAU L, DEAN I, SHI Q, AU A, PARK C, CHEN YY, LIPHARDT J, HWANG ES, WEAVER VM. Human breast cancer invasion and aggression correlates with ECM stiffening and immune cell infiltration. Integr Biol (Camb). 2015

ACETO N, BARDIA A, MIYAMOTO DT, DONALDSON MC, WITTNER BS, SPENCER JA, YU M, PELY A, ENGSTROM A, ZHU H, BRANNIGAN BW, KAPUR R, STOTT SL, SHIODA T, RAMASWAMY S, TING DT, LIN CP, TONER M, HABER DA, MAHESWARAN S. Circulating

tumor cell clusters are oligoclonal precursors of breast cancer metastasis. Cell. 2014; 158:1110–22. [PubMed: 25171411]

APARICIO LA, BLANCO M, CASTOSA R, CONCHA A, VALLADARES M, CALVO L, FIGUEROA A. Clinical implications of epithelial cell plasticity in cancer progression. Cancer Lett. 2015

AXELSON H, FREDLUND E, OVENBERGER M, LANDBERG G, PAHLMAN S. Hypoxia-induced dedifferentiation of tumor cells--a mechanism behind heterogeneity and aggressiveness of solid tumors. Semin Cell Dev Biol. 2005; 16:554–63. [PubMed: 16144692]

BOETTNER B, VAN AELST L. The role of Rho GTPases in disease development. Gene. 2002; 286:155–74. [PubMed: 11943472]

BRAHMBHATT AA, KLEMKE RL. ERK and RhoA differentially regulate pseudopodia growth and retraction during chemotaxis. J Biol Chem. 2003; 278:13016–25. [PubMed: 12571246]

CHAN CE, ODDE DJ. Traction dynamics of filopodia on compliant substrates. Science. 2008; 322:1687–91. [PubMed: 19074349]

CHARRAS G, SAHAI E. Physical influences of the extracellular environment on cell migration. Nature Reviews Molecular Cell Biology. 2014; 15:813–824. [PubMed: 25355506]

CROCKER JC, GRIER DG. Methods of digital video microscopy for colloidal studies. Journal of Colloid and Interface Science. 1996; 179:298–310.

DEAN KM, ROUDOT P, WELF ES, DANUSER G, FIOLKA R. Deconvolution-free Subcellular Imaging with Axially Swept Light Sheet Microscopy. Biophys J. 2015; 108:2807–15. [PubMed: 26083920]

DISCHER DE, JANMEY P, WANG YL. Tissue cells feel and respond to the stiffness of their substrate. Science. 2005; 310:1139–43. [PubMed: 16293750]

FRIEDL P. Prespecification and plasticity: shifting mechanisms of cell migration. Current Opinion in Cell Biology. 2004; 16:14–23. [PubMed: 15037300]

FRIEDL P, LOCKER J, SAHAI E, SEGALL JE. Classifying collective cancer cell invasion. Nat Cell Biol. 2012; 14:777–83. [PubMed: 22854810]

GILKES DM, SEMENZA GL, WIRTZ D. Hypoxia and the extracellular matrix: drivers of tumour metastasis. Nat Rev Cancer. 2014; 14:430–9. [PubMed: 24827502]

GOLUBOVSKAYA VM, NYBERG C, ZHENG M, KWEH F, MAGIS A, OSTROV D, CANCE WG. A small molecule inhibitor, 1,2,4,5-benzenetetraamine tetrahydrochloride, targeting the y397 site of focal adhesion kinase decreases tumor growth. J Med Chem. 2008; 51:7405–16. [PubMed: 18989950]

GUERRERO S, CASANOVA I, FARRE L, MAZO A, CAPELLA G, MANGUES R. K-ras codon 12 mutation induces higher level of resistance to apoptosis and predisposition to anchorage-independent growth than codon 13 mutation or proto-oncogene overexpression. Cancer Res. 2000; 60:6750–6. [PubMed: 11118062]

HANAHAN D, WEINBERG RA. Hallmarks of cancer: the next generation. Cell. 2011; 144:646–74. [PubMed: 21376230]

HARRIS AL. Hypoxia--a key regulatory factor in tumour growth. Nat Rev Cancer. 2002; 2:38–47. [PubMed: 11902584]

HIRATA E, GIROTTI MR, VIROS A, HOOPER S, SPENCER-DENE B, MATSUDA M, LARKIN J, MARAIS R, SAHAI E. Intravital imaging reveals how BRAF inhibition generates drug-tolerant microenvironments with high integrin beta1/FAK signaling. Cancer Cell. 2015; 27:574–88. [PubMed: 25873177]

IHLE NT, BYERS LA, KIM ES, SAINTIGNY P, LEE JJ, BLUMENSCHEIN GR, TSAO A, LIU S, LARSEN JE, WANG J, DIAO L, COOMBES KR, CHEN L, ZHANG S, ABDELMELEK MF, TANG X, PAPADIMITRAKOPOULOU V, MINNA JD, LIPPMAN SM, HONG WK, HERBST RS, WISTUBA II, HEYMACH JV, POWIS G. Effect of KRAS oncogene substitutions on protein behavior: implications for signaling and clinical outcome. J Natl Cancer Inst. 2012; 104:228–39. [PubMed: 22247021]

IRSHAD H, VEILLARD A, ROUX L, RACOCEANU D. Methods for nuclei detection, segmentation, and classification in digital histopathology: a review-current status and future potential. IEEE Rev Biomed Eng. 2014; 7:97–114. [PubMed: 24802905]

KEITH B, SIMON MC. Hypoxia-inducible factors, stem cells, and cancer. Cell. 2007; 129:465–72. [PubMed: 17482542]

KLEMKE RL, CAI S, GIANNINI AL, GALLAGHER PJ, DE LANEROLLE P, CHERESH DA. Regulation of cell motility by mitogen-activated protein kinase. J Cell Biol. 1997; 137:481–92. [PubMed: 9128257]

LEE S, HELFMAN DM. Cytoplasmic p21Cip1 is involved in Ras-induced inhibition of the ROCK/LIMK/cofilin pathway. J Biol Chem. 2004; 279:1885–91. [PubMed: 14559914]

LEVENTAL KR, YU H, KASS L, LAKINS JN, EGEBLAD M, ERLER JT, FONG SF, CSISZAR K, GIACCIA A, WENINGER W, YAMAUCHI M, GASSER DL, WEAVER VM. Matrix crosslinking forces tumor progression by enhancing integrin signaling. Cell. 2009; 139:891–906. [PubMed: 19931152]

LIU YJ, LE BERRE M, LAUTENSCHLAEGER F, MAIURI P, CALLAN-JONES A, HEUZE M, TAKAKI T, VOITURIEZ R, PIEL M. Confinement and low adhesion induce fast amoeboid migration of slow mesenchymal cells. Cell. 2015; 160:659–72. [PubMed: 25679760]

LO CM, WANG HB, DEMBO M, WANG YL. Cell movement is guided by the rigidity of the substrate. Biophys J. 2000; 79:144–52. [PubMed: 10866943]

LOMAKIN AJ, LEE KC, HAN SJ, BUI DA, DAVIDSON M, MOGILNER A, DANUSER G. Competition for actin between two distinct F-actin networks defines a bistable switch for cell polarization. Nat Cell Biol. 2015

MALLIRI A, COLLARD JG. Role of Rho-family proteins in cell adhesion and cancer. Curr Opin Cell Biol. 2003; 15:583–9. [PubMed: 14519393]

MENDOZA MC, ER EE, BLENIS J. The Ras-ERK and PI3K-mTOR pathways: cross-talk and compensation. Trends in Biochemical Sciences. 2011a; 36:320–328. [PubMed: 21531565]

MENDOZA MC, ER EE, ZHANG W, BALLIF BA, ELLIOTT HL, DANUSER G, BLENIS J. ERK-MAPK drives lamellipodia protrusion by activating the WAVE2 regulatory complex. Mol Cell. 2011b; 41:661–71. [PubMed: 21419341]

MENDOZA MC, VILELA M, JUAREZ JE, BLENIS J, DANUSER G. ERK reinforces actin polymerization to power persistent edge protrusion during motility. Science Signaling. 2015:8.

MITRA SK, HANSON DA, SCHLAEPFER DD. Focal adhesion kinase: in command and control of cell motility. Nat Rev Mol Cell Biol. 2005; 6:56–68. [PubMed: 15688067]

MORRIS EJ, JHA S, RESTAINO CR, DAYANANTH P, ZHU H, COOPER A, CARR D, DENG Y, JIN W, BLACK S, LONG B, LIU J, DINUNZIO E, WINDSOR W, ZHANG R, ZHAO S, ANGAGAW MH, PINHEIRO EM, DESAI J, XIAO L, SHIPPS G, HRUZA A, WANG J, KELLY J, PALIWAL S, GAO X, BABU BS, ZHU L, DAUBLAIN P, ZHANG L, LUTTERBACH BA, PELLETIER MR, PHILIPPAR U, SILIPHAIVANH P, WITTER D, KIRSCHMEIER P, BISHOP WR, HICKLIN D, GILLILAND DG, JAYARAMAN L, ZAWEL L, FAWELL S, SAMATAR AA. Discovery of a novel ERK inhibitor with activity in models of acquired resistance to BRAF and MEK inhibitors. Cancer Discov. 2013; 3:742–50. [PubMed: 23614898]

PAWLAK G, HELFMAN DM. Post-transcriptional down-regulation of ROCKI/Rho-kinase through an MEK-dependent pathway leads to cytoskeleton disruption in Ras-transformed fibroblasts. Mol Biol Cell. 2002; 13:336–47. [PubMed: 11809843]

PRIOR IA, LEWIS PD, MATTOS C. A comprehensive survey of Ras mutations in cancer. Cancer Res. 2012; 72:2457–67. [PubMed: 22589270]

PYLAYEVA-GUPTA Y, GRABOCKA E, BAR-SAGI D. RAS oncogenes: weaving a tumorigenic web. Nat Rev Cancer. 2011; 11:761–74. [PubMed: 21993244]

RAJALINGAM K, SCHRECK R, RAPP UR, ALBERT S. Ras oncogenes and their downstream targets. Biochim Biophys Acta. 2007; 1773:1177–95. [PubMed: 17428555]

ROBERTS PJ, STINCHCOMBE TE. KRAS mutation: should we test for it, and does it matter? J Clin Oncol. 2013; 31:1112–21. [PubMed: 23401440]

SAHAI E. Mechanisms of cancer cell invasion. Current Opinion in Genetics & Development. 2005; 15:87–96. [PubMed: 15661538]

SAHAI E, OLSON MF, MARSHALL CJ. Cross-talk between Ras and Rho signalling pathways in transformation favours proliferation and increased motility. EMBO J. 2001; 20:755–66. [PubMed: 11179220]

SANCHEZ-LAORDEN B, VIROS A, GIROTTI MR, PEDERSEN M, SATURNO G, ZAMBON A, NICULESCU-DUVAZ D, TURAJLIC S, HAYES A, GORE M, LARKIN J, LORIGAN P, COOK M, SPRINGER C, MARAIS R. BRAF inhibitors induce metastasis in RAS mutant or inhibitor-resistant melanoma cells by reactivating MEK and ERK signaling. Sci Signal. 2014; 7:ra30. [PubMed: 24667377]

SANZ-MORENO V, GADEA G, AHN J, PATERSON H, MARRA P, PINNER S, SAHAI E, MARSHALL CJ. Rac activation and inactivation control plasticity of tumor cell movement. Cell. 2008; 135:510–23. [PubMed: 18984162]

SATO M, LARSEN JE, LEE W, SUN H, SHAMES DS, DALVI MP, RAMIREZ RD, TANG H, DIMAIO JM, GAO B, XIE Y, WISTUBA II, GAZDAR AF, SHAY JW, MINNA JD. Human lung epithelial cells progressed to malignancy through specific oncogenic manipulations. Mol Cancer Res. 2013; 11:638–50. [PubMed: 23449933]

SCHAFER C, RYMARCZYK G, DING L, KIRBER MT, BOLOTINA VM. Role of molecular determinants of store-operated Ca(2+) entry (Orai1, phospholipase A2 group 6, and STIM1) in focal adhesion formation and cell migration. J Biol Chem. 2012; 287:40745–57. [PubMed: 23043102]

SCHEFFZEK K, AHMADIAN MR, KABSCH W, WIESMULLER L, LAUTWEIN A, SCHMITZ F, WITTINGHOFER A. The Ras-RasGAP complex: structural basis for GTPase activation and its loss in oncogenic Ras mutants. Science. 1997; 277:333–8. [PubMed: 9219684]

SCHUBBERT S, SHANNON K, BOLLAG G. Hyperactive Ras in developmental disorders and cancer. Nat Rev Cancer. 2007; 7:295–308. [PubMed: 17384584]

SEGUIN L, KATO S, FRANOVIC A, CAMARGO MF, LESPERANCE J, ELLIOTT KC, YEBRA M, MIELGO A, LOWY AM, HUSAIN H, CASCONE T, DIAO L, WANG J, WISTUBA II, HEYMACH JV, LIPPMAN SM, DESGROSELLIER JS, ANAND S, WEIS SM, CHERESH DA. An integrin beta3-KRAS-RalB complex drives tumour stemness and resistance to EGFR inhibition. Nat Cell Biol. 2014; 16:457–68. [PubMed: 24747441]

SHUKLA S, ALLAM US, AHSAN A, CHEN GA, KRISHNAMURTHY PM, MARSH K, RUMSCHLAG M, SHANKAR S, WHITEHEAD C, SCHIPPER M, BASRUR V, SOUTHWORTH DR, CHINNAIYAN AM, REHEMTULLA A, BEER DG, LAWRENCE TS, NYATI MK, RAY D. KRAS Protein Stability Is Regulated through SMURF2: UBCH5 Complex-Mediated beta-TrCP1 Degradation. Neoplasia. 2014; 16:115-+. [PubMed: 24709419]

STUPACK DG, CHO SY, KLEMKE RL. Molecular signaling mechanisms of cell migration and invasion. Immunol Res. 2000; 21:83–8. [PubMed: 10852105]

SULZMAIER FJ, JEAN C, SCHLAEPFER DD. FAK in cancer: mechanistic findings and clinical applications. Nat Rev Cancer. 2014; 14:598–610. [PubMed: 25098269]

VAUPEL P, MAYER A. Hypoxia in cancer: significance and impact on clinical outcome. Cancer Metastasis Rev. 2007; 26:225–39. [PubMed: 17440684]

VIKIS H, SATO M, JAMES M, WANG DL, WANG Y, WANG M, JIA DM, LIU Y, BAILEY-WILSON JE, AMOS CI, PINNEY SM, PETERSEN GM, DE ANDRADE M, YANG P, WIEST JS, FAIN PR, SCHWARTZ AG, GAZDAR A, GABA C, ROTHSCHILD H, MANDAL D, KUPERT E, SEMINARA D, VISWANATHAN A, GOVINDAN R, MINNA J, ANDERSON MW, YOU M. EGFR-T790M is a rare lung cancer susceptibility allele with enhanced kinase activity. Cancer Research. 2007; 67:4665–4670. [PubMed: 17510392]

WOLF K, MAZO I, LEUNG H, ENGELKE K, VON ANDRIAN UH, DERYUGINA EI, STRONGIN AY, BROCKER EB, FRIEDL P. Compensation mechanism in tumor cell migration: mesenchymal-amoeboid transition after blocking of pericellular proteolysis. J Cell Biol. 2003; 160:267–77. [PubMed: 12527751]
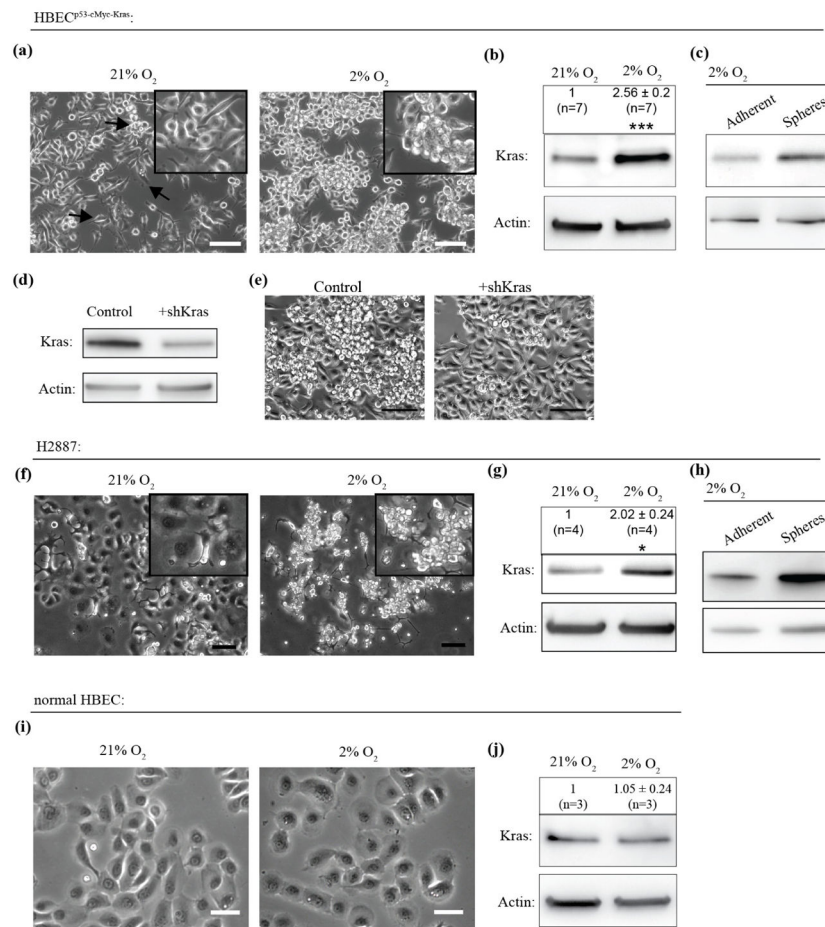
Figure 1. Long-term hypoxia increases oncogenic Kras^{V12} expression levels and sphere-like morphology

(a), Human bronchial epithelial cells transformed with p53 knock-down, Kras^{V12} and cMyc over-expression (HBEC$^{p53-cMyc-Kras}$) change morphological heterogeneity upon long-term (> 4 weeks) cultivation in 2% O_2 compared to 21% O_2. Different cellular morphologies are indicated by black arrows. Scale bar: 100 μm. **(b),** Kras^{V12} expression levels increase upon long-term cultivation in 2% O_2. (***: $P < 0.001$ by Mann-Whitney test, ±: standard error). n indicates number of data points. **(c),** Spheres are higher in Kras^{V12} protein levels. **(d),** Kras^{V12} levels decrease after knock-down using shRNA against total (wild-type and mutated) Kras in HBEC$^{p53-cMyc-Kras}$ cultured in 2% O_2. **(e),** This treatment leads to decrease of sphere-like morphology. Scale bar: 100 μm. **(f),** Lung cancer cell line H2887 bearing Kras^{V12} mutation shows morphological heterogeneity grown in 21% O_2 with adherent and sphere-like cells. Upon long-term cultivation in 2% O_2 cellular sphere-like morphology increases. Scale bar: 100 μm. **(g),** Kras^{V12} levels significantly increase in long-term hypoxia. (*: $P < 0.05$ by Mann-Whitney test, ±: standard error). n indicates number of data points. **(h),** Higher Kras^{V12} protein levels in spheres. **(i),** Normal, untransformed HBECs show homogeneous morphology which does not change upon long-term cultivation in 2% O_2. Scale bar: 50 μm. **(j),** Long-term hypoxia does not affect Kras protein levels. (non-significant by Mann-Whitney test, ±: standard error). n indicates number of data points.
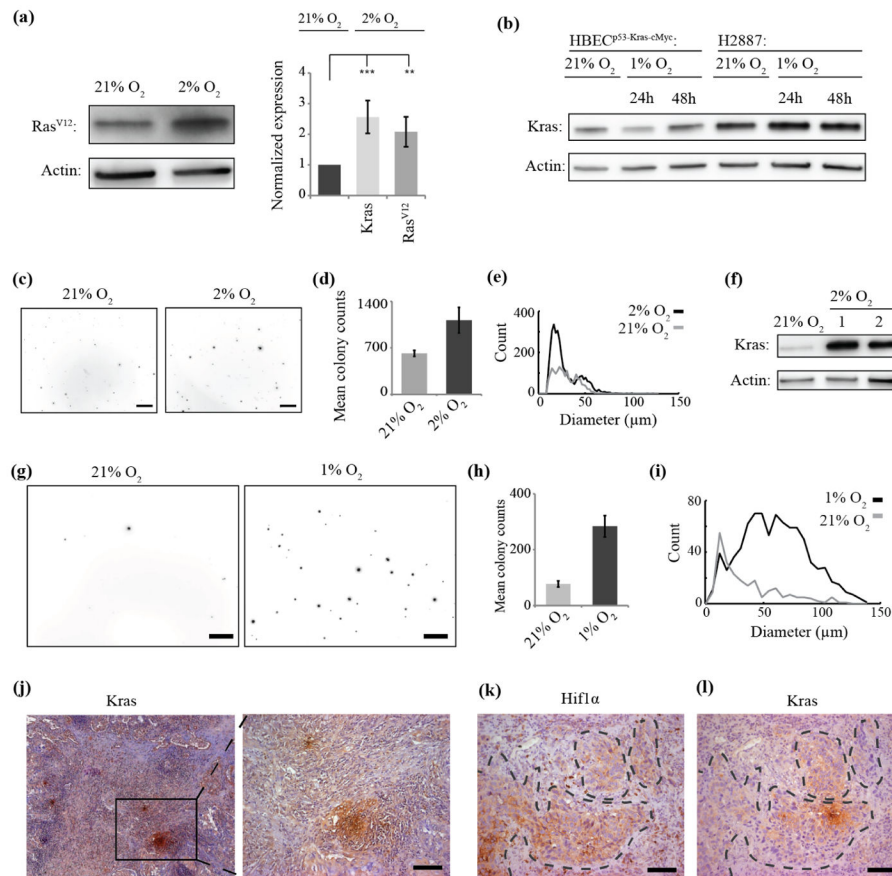
Figure 2. Upregulation of Kras^{V12} in long-term hypoxia increases tumorigenicity *in vitro* and is correlated with hypoxia areas *in vivo*

(a), Ras^{V12}-specific antibody was used to confirm Kras^{V12} upregulation in HBEC$^{p53\text{-}cMyc\text{-}Kras}$ upon 2% O_2. Quantification comparing total Kras and mutated Kras^{V12} shows similar increase in 2% O_2 indicating major role of hypoxia-induced Kras^{V12} upregulation. Error bars show standard error. (**: $P < 0.01$, ***: $P < 0.001$ by ANOVA-test). **(b),** Short-term (24–48 h) exposure to hypoxia does not significantly increase Kras^{V12} expression in HBEC$^{p53\text{-}cMyc\text{-}Kras}$ and H2887. **(c),** Maximum intensity projections of z-stacks of soft-agar colonies formed in 21% or 2% O_2 show increased tumorigenic potential upon hypoxia in HBEC$^{p53\text{-}cMyc\text{-}Kras}$. Scale bar: 500 μm. **(d),** Number of soft-agar colonies of HBEC$^{p53\text{-}cMyc\text{-}Kras}$ increases in 2% O_2. (n=3, error bars show standard deviation). **(e),** The proportion of larger colonies of HBEC$^{p53\text{-}cMyc\text{-}Kras}$ increases in 2% O_2. **(f),** Analysis of Kras^{V12} levels shows high levels for two soft-agar colonies isolated from the 2% assay compared to HBEC$^{p53\text{-}cMyc\text{-}Kras}$ grown in 21% O_2. **(g),** Maximum intensity projections of z-stacks of soft-agar colonies formed in 21% or 1% O_2 show increased tumorigenic potential upon hypoxia in H2887 cells. Scale bar: 500 μm. **(h),** The number of soft-agar colonies of H2887 cells increases in 1% O_2. (n=3, error bars show standard deviation). **(i),** The proportion of larger colonies of H2887 cells increases in 1% O_2. **(j),** Kras^{V12} expression is heterogeneous *in vivo* as observed by staining for Kras in lung tumor sections positive for Kras^{V12} mutation. Scale bar: 100 μm. **(k), (l),** Localization of Kras^{V12} hotspots overlays with hypoxic areas in the tumor as identified by Hif1α (**k**) and Kras (**l**) staining in

consecutive lung tumor slides. Hif1α positive areas were outlined (**k**) and overlay with Kras in (**l**). Scale bars: 100 μm.
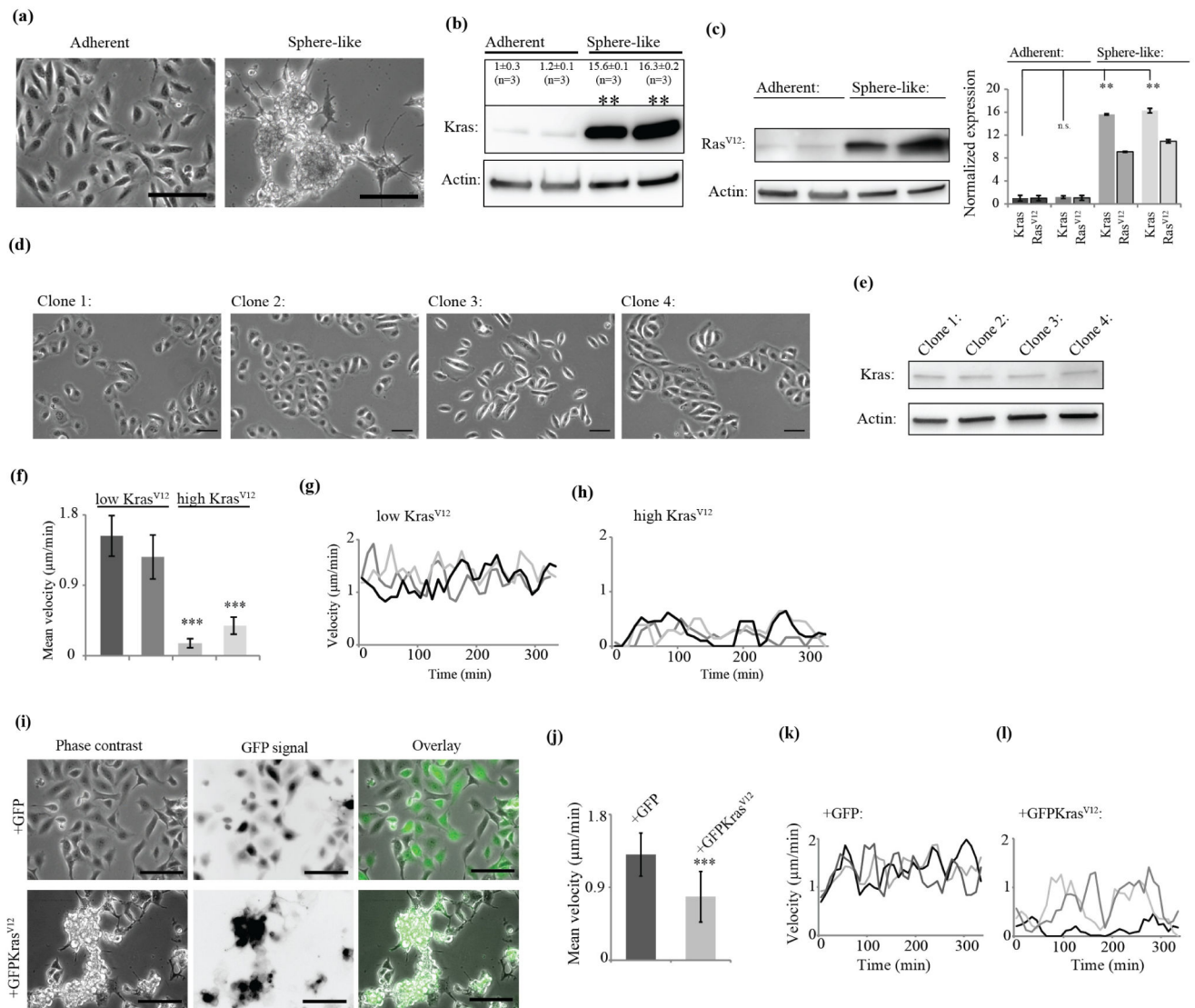
Figure 3. Differential levels of oncogenic Kras^V12 control cell morphology and migration

(a), Clonal separation of HBEC^p53-cMyc-Kras reveals clones with adherent and sphere-like morphologies. Scale bar: 100 μm. **(b),** Morphologies of clones correlate with Kras protein levels. (**: P < 0.01 by ANOVA-test, ±: standard error). n indicates number of data points. **(c),** Expression of Kras^V12 was confirmed using a mutation specific Ras^V12 antibody in adherent and sphere-like clones. Comparison of Kras^V12 (using a Ras^V12-specific antibody) and general Kras levels (using an antibody recognizing wild type and mutated forms) indicates that the expression increase between adherent and sphere-like clones is predominantly related to expression increase of the mutant form. Error bars show standard error. (**: P < 0.01 by ANOVA-test, n.s.: not significant, n=3, for Ras^V12 of first low Kras^V12 clone: n=2). **(d),** Clonal isolation of normal, immortalized HBECs (Human Bronchial Epithelial Cell) produced clones with homogeneous, adherent morphology. Scale bar: 50 μm. **(e),** Kras levels are stable between clones from normal HBECs. **(f),** Analysis of random migration of high Kras^V12 clones (n=39 and 50) and low Kras^V12 clones (both

n=50). (***: $P < 0.001$ by Student's t-test). Error bars show standard deviation. **(g),** Migration velocities of three representative cells from a low Kras^{V12} clone are displayed. **(h),** Migration velocities of three representative cells from a high Kras^{V12} clone are displayed. **(i),** Morphology of adherent, low Kras^{V12} clones isolated from HBEC$^{p53-cMyc-Kras}$ switches to sphere-like upon exogenous over-expression of GFPKras^{V12}. The switch is not observed when infected with empty GFP vector as control. Scale bar: 100 μm. **(j),** Comparison of velocities of low Kras^{V12} clones infected with either empty GFP vector (n=59) or GFPKras^{V12} (n=59). (***: $P < 0.001$ by Mann-Whitney test). Error bars show standard deviation. **(k),** Migration velocities of three representative cells from a low Kras^{V12} clone infected with GFP control vector. **(l),** Migration velocities of three representative cells from a low Kras^{V12} clone infected with GFPKras^{V12} are displayed. **(a)-(l)** All experiments were performed in 2% O_2.
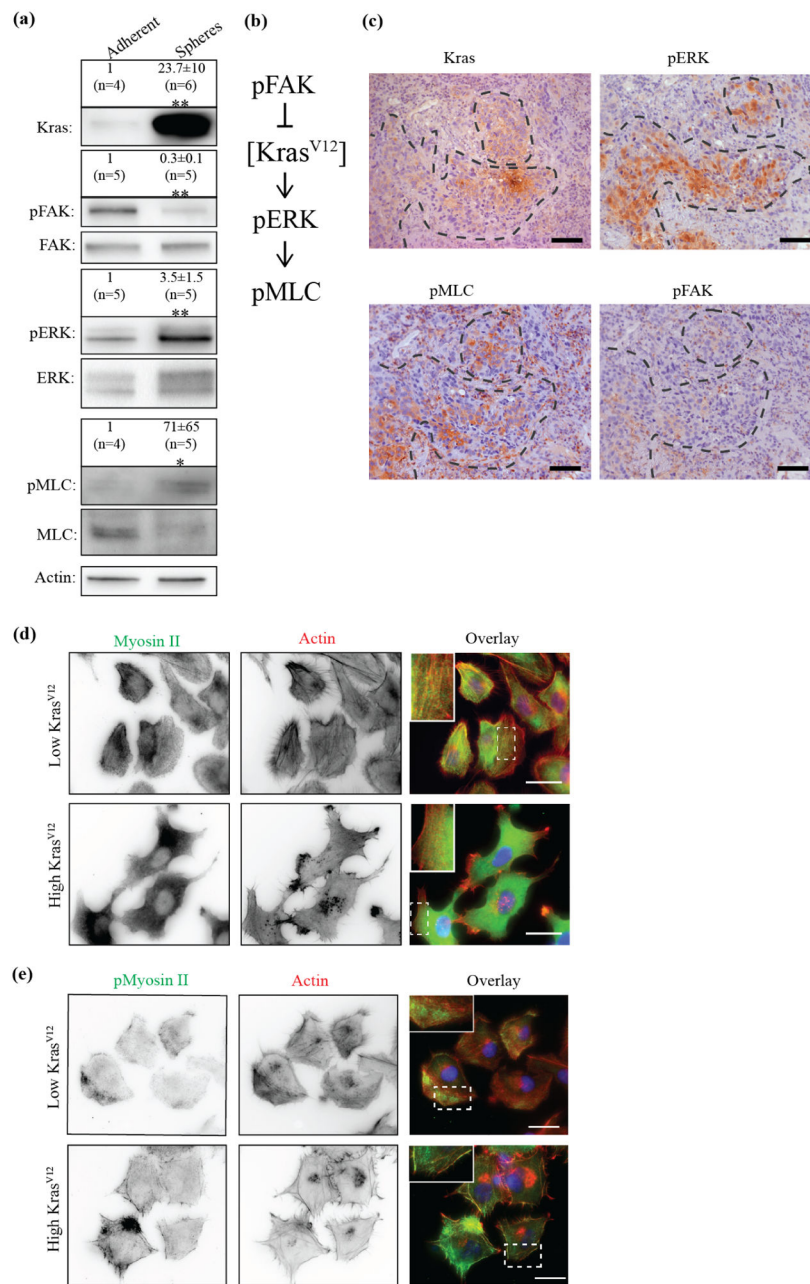
Figure 4. Differential activation of FAK/ERK/Myosin II signaling pathway and altered cellular polarity and cytoskeleton distribution in high and low Kras^{V12} clones

(a), Comparison of signaling profile of adherent and sphere-like HBEC$^{p53\text{-}cMyc\text{-}Kras}$ population. In a western blot, high Kras^{V12} spheres show less FAK activation (pFAK/FAK) but increased ERK (pERK/ERK) and Myosin II (pMLC/MLC, MLC: Myosin Light Chain) activity. (*: P < 0.05, **: P < 0.01 by Mann-Whitney test, ±: standard error). n indicates number of data points. **(b),** Proposed signaling cascade consistent with data in (**a**). **(c),** Consecutive lung tumor sections tested positive for Kras^{V12} mutation were stained for pERK, pMLC and pFAK and compared to areas positive for Kras^{V12} expression (same picture also shown in figure 2(l)). Areas positive for Kras^{V12} signal show elevated staining

of pERK and pMLC and low staining for pFAK. Conserved tumor structures throughout the slides are indicated with the dashed line. Scale bars: 100 μm. **(d),** Cells from low or high Kras[V12] clones were fixed and stained for Myosin II (green in overlay) and Actin (red in overlay). Nuclei were visualized by Hoechst (blue in overlay). Low Kras[V12] cells show typical polarization for effective migration with Actin-rich lamellipodium in the front and actomyosin-rich back. Such polarity is lost in high Kras[V12] cells which show multiple lamellipodial initiation sites and an asymmetric Myosin II distribution. Zoomed inlets show punctuated Myosin localization along actin filaments. Scale bars: 20 μm. **(e),** Similar distribution is also observed by staining for phosphorylated Myosin (pMyosin II). Scale bars: 20 μm. **(a), (d), (e)** All experiments were performed in 2% O_2.
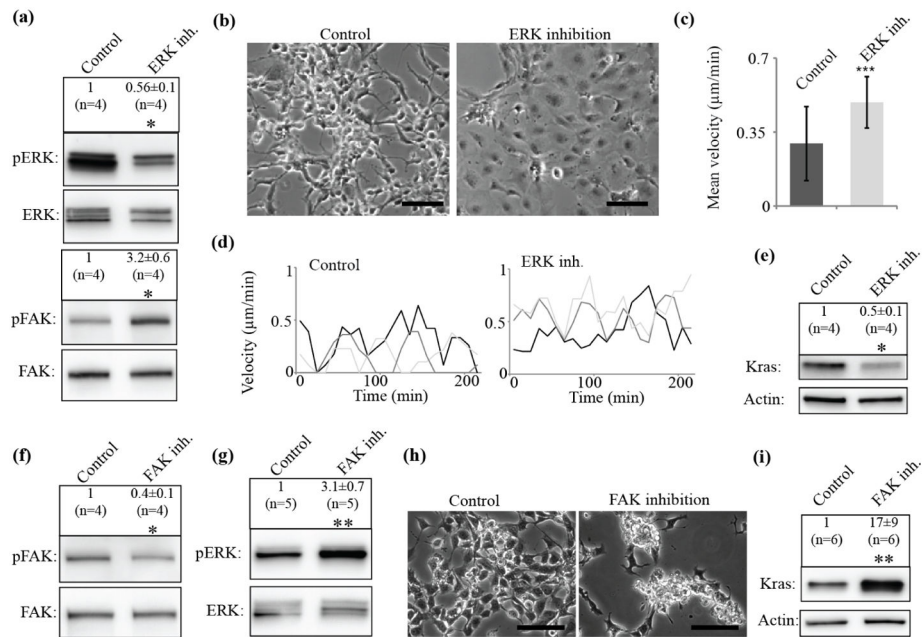
Figure 5. Reduction of ERK and FAK signaling converts clonal phenotypes and Kras^{V12} levels
(a), High Kras^{V12} cells were treated with DMSO as control (Control) or with SCH772984 (ERK inh.), a specific ERK inhibitor, and protein extracts were analyzed for ERK activation by western blot and ratio analysis of phosphorylated ERK (pERK) and total ERK (ERK). Treatment with ERK inhibitor led to decrease in ERK activation. Such treatment also led to activation of FAK (focal adhesion kinase) signaling measured by western blot and ratio analysis of phosphorylated FAK (pFAK) to total FAK (FAK). (*: $P < 0.05$ by Mann-Whitney test, ±: standard error). n indicates number of data points. **(b),** Treatment of high Kras^{V12} sphere-like clones with the ERK inhibitor (ERK inh.) causes a switch to adherent morphology. Scale bar: 100 μm. **(c),** Comparison of migration velocities of control (n=50) and ERK inh. treated (n=40) cells. (***: $P < 0.001$ by Mann-Whitney test). Error bars show standard deviation. **(d),** High Kras^{V12} cells (control) switch migration behavior to more persistent movement upon ERK inhibition (ERK inh.). Shown are migration velocities of three representative cells from control or ERK-inhibited high Kras^{V12} cells. **(e),** Kras^{V12} levels decrease upon ERK inh. (*: $P < 0.05$ by Mann-Whitney test, ±: standard error). n indicates number of data points. **(f),** Low Kras^{V12} cells were treated with DMSO as control (Control) or with a specific FAK (focal adhesion kinase) inhibitor (FAK inh.), and protein extracts were analyzed for FAK signaling by western blot and ratio analysis of phosphorylated FAK (pFAK) and total FAK (FAK). Treatment with FAK inhibitor led to decrease in FAK activation. (*: $P < 0.05$ by Mann-Whitney test, ±: standard error). n indicates number of data points. **(g),** Such treatment also led to activation of ERK signaling measured by western blot and ratio analysis of phosphorylated ERK (pERK) to total ERK (ERK). (**: $P < 0.01$ by Mann-Whitney test, ±: standard error). n indicates number of data points. **(h),** FAK inhibition in low Kras^{V12} adherent clones leads to sphere formation. Scale bar: 100 μm. **(i),** Increase in Kras^{V12} expression levels upon FAK inhibition. (**: $P < 0.01$ by Mann-Whitney test, ±: standard error). n indicates number of data points. **(a)-(i)** All experiments were performed in 2% O_2.
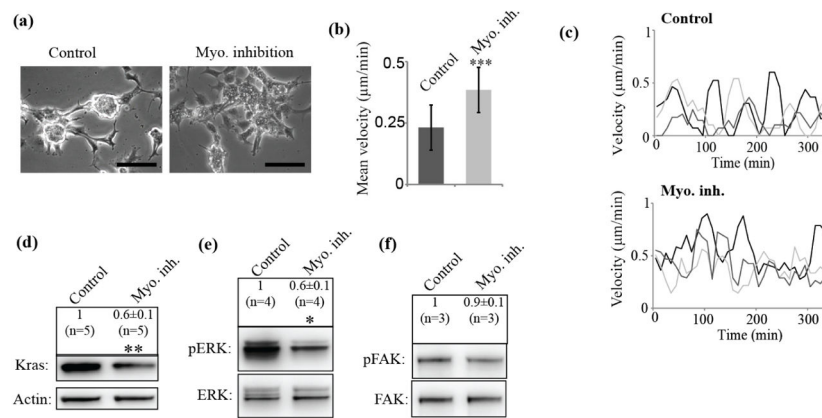
Figure 6. Myosin inhibition switches clonal phenotype to adherent and motile with decreased Kras^{V12} levels

(a), Treatment of high Kras^{V12} sphere-like clones with Myosin inhibitor causes formation of more adherent phenotype. Scale bar: 100 μm. **(b),** Analysis of migration velocities of control (n=74) and Myosin inhibitor-treated (Myo. inh.) cells (n=80). (***: $P < 0.001$ by Mann-Whitney test). Error bars show standard deviation. **(c),** High Kras^{V12} cells switch migration behavior to more persistent movement upon Myosin II inhibition (Myo. inh.). Shown are migration velocities of three representative cells from control or blebbistatin-treated high Kras^{V12} cells. **(d),** This went along with a decrease in Kras^{V12} levels. (**: $P < 0.01$ by Mann-Whitney test, ±: standard error). n indicates number of data points. **(e),** Such treatment led to reduction in ERK activation measured by western blot and ratio analysis of phosphorylated ERK (pERK) to total ERK (ERK). (*: $P < 0.05$ by Mann-Whitney test, ±: standard error). n indicates number of data points. **(f),** No change of FAK signaling was observed by western blot and ratio analysis of phosphorylated FAK (pFAK) and total FAK (FAK). (±: standard error). n indicates number of data points. **(a)-(f)** All experiments were performed in 2% O_2
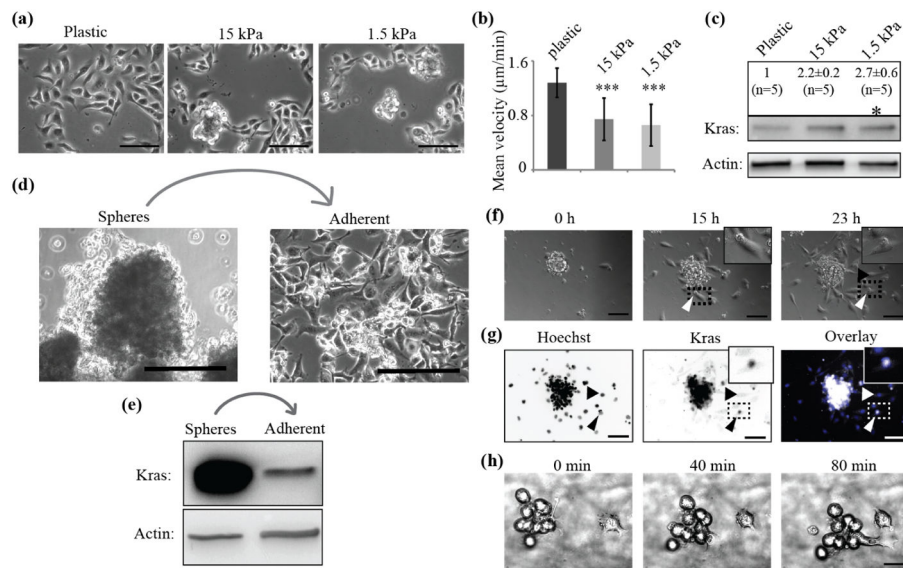
Figure 7. Oncogenic Kras^{V12} expression is controlled by a mechano-sensitive switch determining cell morphology and migration

(a), Adherent, low Kras^{V12} clones on surfaces with varying stiffness (plastic, 15 kPa and 1.5 kPa) form aggregates on soft (15 and 1.5 kPa) but not on stiff (plastic) substrates. Scale bar, 100 μm. **(b),** Migration velocities of adherent clones on 15 kPa (n=57) or 1.5 kPa (n=60) substrates compared to plastic (n=60). (***: $P < 0.001$ by Student's t-test). Error bars show standard deviation. **(c),** Kras^{V12} levels increase on soft substrates. (*: $P < 0.05$ by ANOVA-test, ±: standard error). n indicates number of data points. **(d),** Transfer of high Kras^{V12} spheres onto attachment, plastic dishes initiates adherent phenotype and migration. Scale bar, 100 μm. **(e),** Culture on adhesive surfaces leads to reduction in Kras^{V12} expression. **(f),** Live cell imaging of dissemination from spheres over a time period of 23 h shows rapid initiation of adhesion and motility. Non-motile, round cells get transported out by adherent, motile cells which stay connected over the whole period of observation (arrow heads, zoomed inlet, Movie14). Scale bar, 50 μm. **(g),** After 23 h cells were fixed and stained for nuclei (Hoechst, blue) and Kras (white). Kras^{V12} levels in non-motile, cargo cells are high (arrow heads, zoomed inlet). Scale bar, 50 μm. **(h),** Live cell imaging in 3D collagen matrix shows conjoint migration of clusters of motile, spread and non-motile, spherical cells (Movie16). Scale bar, 50 μm. **(a)–(g)** All experiments were performed in 2% O$_2$.